# Influenza A virus RNA polymerase structures provide insights into viral genome replication

Haitian Fan[1,8], Alexander P Walker[1,8], Loïc Carrique[2,8], Jeremy R Keown[2,8], Itziar Serna Martin[1,2,6], Dimple Karia[2], Jane Sharps[1], Narin Hengrung[1,2,7], Els Pardon[3], Jan Steyaert[4], Jonathan M Grimes[2,5,9*] and Ervin Fodor[1,9*]

[1]Sir William Dunn School of Pathology, University of Oxford, South Parks Road, Oxford OX1 3RE, United Kingdom

[2]Division of Structural Biology, Henry Wellcome Building for Genomic Medicine, University of Oxford, Oxford OX3 7BN, United Kingdom

[3]VIB-VUB Center for Structural Biology, VIB, 1050 Brussels, Belgium

[4]Structural Biology Brussels, Vrije Universiteit Brussel, 1050 Brussels, Belgium

[5]Diamond Light Source Ltd, Harwell Science & Innovation Campus, Didcot OX11 0DE, United Kingdom

[6]Present address: Crystal and Structural Chemistry, Bijvoet Center for Biomolecular Research, Department of Chemistry, Faculty of Science, Utrecht University, Padualaan 8, 3584 CH, Utrecht, The Netherlands

[7]Present address: Francis Crick Institute, 1 Midland Road, Kings Cross, London NW1 1AT, United Kingdom

[8]These authors contributed equally: Haitian Fan, Alexander Walker, Loïc Carrique, Jeremy R Keown

[9]These authors jointly supervised this work: Jonathan M Grimes, Ervin Fodor

[*]email: jonathan@strubi.ox.ac.uk, ervin.fodor@path.ox.ac.uk

**Influenza A viruses (IAV) are responsible for seasonal epidemics, and pandemics can arise from novel zoonotic influenza A viruses transmitting to humans[1,2]. IAV contain a segmented negative sense RNA genome that is transcribed and replicated by the viral RNA-dependent RNA polymerase, composed of the PB1, PB2, and PA subunits[3-5]. Although the high-resolution crystal structure of bat IAV polymerase ($FluPol_A$) has been reported[6], there are no complete structures available for human and avian $FluPol_A$. Furthermore, the molecular mechanisms of viral RNA (vRNA) replication, which proceeds through a complementary RNA (cRNA) replicative intermediate and requires polymerase oligomerisation[7-10], remain largely unknown. Here we report 3.0 – 4.3 Å resolution structures of polymerases from human A/NT/60/1968 (H3N2) and avian A/duck/Fujian/01/2002 (H5N1) IAVs, obtained by crystallography and cryo-electron microscopy (cryo-EM), in the presence or absence of cRNA or vRNA template. In solution, $FluPol_A$ forms dimers of heterotrimers through the PA C-terminal domain and the PB1 thumb and PB2 N1 subdomains. A cryo-EM structure of a monomeric $FluPol_A$, bound to cRNA template, reveals a binding site for the 3′ cRNA at the dimer interface. Using a combination of cell-based and *in vitro* assays we show that the $FluPol_A$ dimer interface is required for initiation of vRNA synthesis during viral genome replication. Furthermore, we show that a nanobody, a single-domain antibody, which interferes with $FluPol_A$ dimerisation, inhibits vRNA synthesis and consequently virus replication in infected cells. Our study provides the first high-resolution structures of medically relevant $FluPol_A$ and offers novel insights into the replication mechanisms of the viral RNA genome. Furthermore, it identifies novel sites of $FluPol_A$ that could be targeted for antiviral drug development.**

We used x-ray crystallography to solve the complete apo structures of human and avian $FluPol_A$ at 3.32 Å and 3.63 Å resolution, respectively (Extended Data Fig. 1a-f, Extended Data Table 1, Supplementary Fig. 1). Human and avian $FluPol_A$ are essentially identical structures forming dimers of heterotrimers with dimerisation mediated by the PA C-terminal domain, the PB1 thumb and PB2 N1 subdomains (Fig. 1a, b, Extended Data Fig. 1g-i). A key feature of this dimer interface is loop 352-356 in the PA C-terminal domain that interacts with the same loop of the second polymerase (Fig. 1c, Extended Data Fig. 1g). The dimer interface also involves hydrogen bonds between the PA C-terminal domain and PB2 N1 (Fig. 1d, Extended Data Fig. 1h). Mutation of PA residues 352-356 to alanines ($PA_{352\text{-}356A}$) resulted in a shift towards a monomeric $FluPol_A$ heterotrimer (Extended Data Fig. 2a).

FluPol$_A$ dimerisation through the same interface was also observed in mammalian cells (Extended Data Fig. 2b) and in previous studies of a truncated avian FluPol$_A$[11].

To assess the importance of dimerisation for FluPol$_A$ function we used a minireplicon assay measuring viral transcription and replication in the context of viral ribonucleoprotein complexes (vRNPs) (Fig. 2a). The PA$_{352\text{-}356A}$ dimer interface mutation and mutations designed to destabilise PB2 loop 71-76 and PA loop 352-356 at the dimer interface significantly decreased the synthesis of all viral RNAs (Fig. 2b, Extended Data Fig. 2c). Co-expression of PA$_{352\text{-}356A}$ with PA$_{D108A}$, a transcription-deficient but replication-competent polymerase[12,13], lead to a significant increase in mRNA signal, indicating that the PA$_{352\text{-}356A}$ mutant is specifically deficient in viral genome replication (Fig. 2b). In agreement, the PA$_{352\text{-}356A}$ mutation did not inhibit transcription *in vitro* using a vRNA template and capped RNA primer (Fig. 2c). It did not affect primer-independent cRNA synthesis on a vRNA template either but was deficient in vRNA synthesis on a cRNA template (Fig. 2d, e) that involves pppApG synthesis at positions 4 and 5 and subsequent realignment of the template[14]. In ApG dinucleotide-primed assays, the PA$_{352\text{-}356A}$ mutant showed activity on both vRNA and cRNA templates but on the cRNA template promoted the formation of a short 12 nucleotide and other incorrectly initiated products (Extended Fig. 2d, e). The ratio of full-length 15 to the short 12 nucleotide product was dependent on FluPol$_A$ concentration, and could be increased by adding a polymerase active site mutant (PB1a), suggesting the involvement of an intermolecular interaction between polymerases (Extended Data Fig. 2f, g). These data show that the FluPol$_A$ dimer interface is important for initiation of vRNA synthesis on the cRNA template and suggest that dimerisation promotes stabilisation of the replication complex and the correct positioning of the cRNA template to allow terminal pppApG-primed initiation during vRNA synthesis.

To investigate the binding of FluPol$_A$ to the cRNA template we determined the structure of dimeric FluPol$_A$ in the presence of cRNA promoter (comprised of 5′ and 3′ cRNA termini)[3,4] at 4.07 Å resolution using cryo-EM (Fig. 3a, Extended Data Fig. 3a-f, Extended Data Table 2). Although the PA endonuclease and PB2 C-terminal domains could not be resolved, in agreement with previous observations that these domains are flexible[15-17], unambiguous density was observed for the dimer interface, revealing a dimer interface essentially identical to that in the FluPol$_A$ crystal structures (Fig. 1a). Only the 5′ cRNA was clearly resolved in the density maps, showing a hook structure bound in a pocket formed by PA and PB1, as observed in previous FluPol structures with 5′ vRNA and cRNA[6,16,18].

Unresolved density around the template entry channel was observed suggesting that the 3′ cRNA has entered the active site but is highly dynamic (Extended Data Fig. 3g, h). These results confirm that cRNA-bound $FluPol_A$ can form dimers in solution.

To gain further insight into $FluPol_A$ dimerisation and cRNA binding we used a nanobody (Nb8205) raised against $FluPol_A$ that reduces $FluPol_A$ dimerisation (Extended Data Fig. 4a-c). A crystal structure of the apo $FluPol_A$-Nb8205 complex solved at 3.34 Å resolution revealed that the complementarity determining regions (CDRs) of Nb8205 interact with $FluPol_A$ at the PA C-terminal domain and PB1 thumb, a site close to the dimer interface (Extended Data Fig. 4d, e, Extended Data Table 1). We also solved the structures of monomeric and dimeric $FluPol_A$ bound to Nb8205 and cRNA promoter at 3.79 and 4.15 Å resolution, respectively, using cryo-EM (Fig. 3b, Extended Data Fig. 5a-h, Extended Data Table 2). The structure of the Nb8205-bound $FluPol_A$ dimer is essentially identical to the dimer observed in the absence of Nb8205, showing the same binding mode for the 5′ cRNA terminus with unresolved density around the template entry channel suggesting the presence of a dynamic 3′ cRNA terminus in the active site (Extended Data Fig. 5i). In contrast, the structure of the Nb8205-bound $FluPol_A$ monomer revealed the binding of both the 5′ and 3′ cRNA termini (Fig. 3b, Supplementary Video 1). The 5′ cRNA terminus is bound in the hook conformation as observed in the $FluPol_A$ dimer, while the 3′ cRNA terminus occupies a binding site formed between the PA C-terminal domain and the PB1 thumb and PB2 N1 subdomains. Only bases 4 to 8 of the 15 nucleotide 3′ cRNA could be resolved which are coordinated by residues of PB1 loop 553-571 and a series of charged residues of PA (E300, Y464, K488, R496) (Fig. 3c, Supplementary Video 1). We observed the same binding site for 3′ cRNA in a cryo-EM structure of the monomeric form of influenza B virus polymerase ($FluPol_B$) (Extended Data Fig. 6a-f). This 3′ cRNA binding site lies in close vicinity to the $FluPol_A$ dimer interface (Extended Data Fig. 6g) and could represent a docking site for the 3′ cRNA in the replication pre-initiation state of $FluPol_A$ and could also accommodate the 3′ cRNA during replication elongation, after it is copied and extruded through the template exit channel. This site is distinct from the previously observed 3′ vRNA binding site in structures of bat $FluPol_A$ and human $FluPol_B$ but lies in a similar position as the 3′ vRNA of the La Crosse orthobunyavirus RNA polymerase (Extended Data Fig. 6h)[6,18,19].

A comparison of the monomeric and dimeric $FluPol_A$ structures in complex with Nb8205 revealed that dimerisation induces a movement of a helical bundle formed by the PB1 thumb and PB2 N1 subdomains (Fig. 3d, Supplementary Video 2). This movement

results in an opening of the 3′ cRNA binding site explaining the absence of 3′ cRNA at this site in the dimeric structure. Furthermore, dimerisation leads to rearrangements in the polymerase active site that could destabilise the 3′ cRNA binding, in agreement with the lack of density for the 3′ extremity of the 3′ cRNA in the dimer structure (Extended Data Fig. 5i). Specifically, the visible residues closest to the tip of the priming loop (PB1 residues E638 and M656) are moved away from the active site by approximately 7 Å, presumably pulling the tip out by a similar distance (Extended Data Fig. 6i, Supplementary Video 3). This movement of the priming loop and the destabilised binding of the 3′ cRNA could facilitate backtracking of the cRNA template during the initiation of vRNA synthesis, in agreement with previous data that the priming loop is required during the realignment of the pppApG initiating dinucleotide to the cRNA terminus[20,21]. In further support of this model we have solved the structure of $FluPol_A$ bound to the vRNA promoter and capped RNA by cryo-EM at 3.0 Å resolution (Extended Data Fig. 7a-f). This structure, with the flexible PA endonuclease and PB2 C-terminal domains fully resolved, revealed the interaction of a fully resolved priming loop with the 3′ vRNA in the active site (Extended Data Fig. 7g). The priming loop acts to buttress the template RNA positioning it next the catalytic aspartates (PB1 amino acid residues D445 and D446) to allow terminal initiation. This interaction is mediated by PB1 amino acid P651 at the tip of the priming loop that was found to be critical for priming loop function in our previous study[21]. The observed buttressing of the template by the priming loop is consistent with our proposed model for template realignment for vRNA synthesis triggered by polymerase dimerisation (Extended Data Fig. 7h, Supplementary Video 4).

To address the effect of Nb8205 on $FluPol_A$ function, co-expression of Nb8205 in a minireplicon assay severely inhibited the accumulation of all viral RNAs, while another nanobody (Nb8210), also raised against $FluPol_A$ but not affecting $FluPol_A$ dimerisation (Extended Data Fig. 4a-c), had no significant effect (Fig. 4a). Nb8205 had no effect on capped RNA-primed transcription or cRNA synthesis on a vRNA template, but strongly inhibited vRNA synthesis on a cRNA template *in vitro* (Fig. 4b-d). Addition of Nb8205 to ApG dinucleotide-primed assays did not reduce activity but resulted in incorrectly initiated vRNA products on the cRNA template (Extended Data Fig. 8a-c). Nb8205 inhibited vRNA accumulation at 16 to 32 hours post-infection in cells infected with influenza A/WSN/33 virus and caused a significant reduction in virus titre, while Nb8210 had no or a much smaller effect (Fig. 4e).

Collectively, these data show that $FluPol_A$ dimerisation is required for the initiation of vRNA synthesis on the cRNA template during viral genome replication (Fig. 4f). Replication initiation on the cRNA template being dependent on dimerisation is consistent with our previous observations that vRNA synthesis requires a trans-activating polymerase[8]. A requirement for trans-activation through polymerase dimerisation provides an elegant mechanism for tuning the amount of vRNA synthesised - only once there is a sufficient level of newly-made free polymerase available in the cell is vRNA production initiated. This could help ensure that the virus does not produce vRNA that cannot be assembled into vRNPs and therefore could trigger an antiviral response through recognition by pathogen recognition receptors, e.g. RIG-I[22,23]. It is interesting to note that numerous avian to mammalian adaptive mutations have been observed at the dimer interface suggesting that dimerisation of $FluPol_A$ may be regulated in a host-specific manner (Extended Data Fig. 8d). In conclusion, the complete high-resolution structures of medically relevant human and avian $FluPol_A$ and the identification of novel sites involved in polymerase dimerisation and cRNA promoter binding will provide guidance for the development of influenza antivirals.

## REFERENCES


1. Taubenberger, J.K. & Kash, J.C. Influenza virus evolution, host adaptation, and pandemic formation. *Cell Host Microbe* **7**, 440-51 (2010).
2. Mostafa, A., Abdelwhab, E.M., Mettenleiter, T.C. & Pleschka, S. Zoonotic Potential of Influenza A Viruses: A Comprehensive Overview. *Viruses* **10**(2018).
3. Pflug, A., Lukarska, M., Resa-Infante, P., Reich, S. & Cusack, S. Structural insights into RNA synthesis by the influenza virus transcription-replication machine. *Virus Res* **234**, 103-117 (2017).
4. Te Velthuis, A.J. & Fodor, E. Influenza virus RNA polymerase: insights into the mechanisms of viral RNA synthesis. *Nat Rev Microbiol* **14**, 479-93 (2016).
5. Walker, A.P. & Fodor, E. Interplay between Influenza Virus and the Host RNA Polymerase II Transcriptional Machinery. *Trends Microbiol* **27**, 398-407 (2019).
6. Pflug, A., Guilligay, D., Reich, S. & Cusack, S. Structure of influenza A polymerase bound to the viral RNA promoter. *Nature* **516**, 355-60 (2014).
7. Jorba, N., Coloma, R. & Ortin, J. Genetic trans-complementation establishes a new model for influenza virus RNA transcription and replication. *PLoS Pathog* **5**, e1000462 (2009).
8. York, A., Hengrung, N., Vreede, F.T., Huiskonen, J.T. & Fodor, E. Isolation and characterization of the positive-sense replicative intermediate of a negative-strand RNA virus. *Proc Natl Acad Sci U S A* **110**, E4238-E4245 (2013).
9. Jorba, N., Area, E. & Ortin, J. Oligomerization of the influenza virus polymerase complex in vivo. *J Gen Virol* **89**, 520-4 (2008).
10. Moeller, A., Kirchdoerfer, R.N., Potter, C.S., Carragher, B. & Wilson, I.A. Organization of the influenza virus replication machinery. *Science* **338**, 1631-4 (2012).

11. Chang, S. et al. Cryo-EM structure of influenza virus RNA polymerase complex at 4.3 A resolution. *Mol Cell* **57**, 925-935 (2015).
12. Hara, K., Schmidt, F.I., Crow, M. & Brownlee, G.G. Amino acid residues in the N-terminal region of the PA subunit of influenza A virus RNA polymerase play a critical role in protein stability, endonuclease activity, cap binding, and virion RNA promoter binding. *J Virol* **80**, 7789-98 (2006).
13. Manz, B., Brunotte, L., Reuther, P. & Schwemmle, M. Adaptive mutations in NEP compensate for defective H5N1 RNA replication in cultured human cells. *Nat Commun* **3**, 802 (2012).
14. Deng, T., Vreede, F.T. & Brownlee, G.G. Different de novo initiation strategies are used by influenza virus RNA polymerase on its cRNA and viral RNA promoters during viral RNA replication. *J Virol* **80**, 2337-48 (2006).
15. Hengrung, N. et al. Crystal structure of the RNA-dependent RNA polymerase from influenza C virus. *Nature* **527**, 114-7 (2015).
16. Thierry, E. et al. Influenza Polymerase Can Adopt an Alternative Configuration Involving a Radical Repacking of PB2 Domains. *Mol Cell* **61**, 125-37 (2016).
17. Serna Martin, I. et al. A Mechanism for the Activation of the Influenza Virus Transcriptase. *Mol Cell* **70**, 1101-1110 e4 (2018).
18. Reich, S. et al. Structural insight into cap-snatching and RNA synthesis by influenza polymerase. *Nature* **516**, 361-6 (2014).
19. Gerlach, P., Malet, H., Cusack, S. & Reguera, J. Structural Insights into Bunyavirus Replication and Its Regulation by the vRNA Promoter. *Cell* **161**, 1267-79 (2015).
20. Oymans, J. & Te Velthuis, A.J.W. A Mechanism for Priming and Realignment during Influenza A Virus Replication. *J Virol* **92**(2018).
21. Te Velthuis, A.J., Robb, N.C., Kapanidis, A.N. & Fodor, E. The role of the priming loop in influenza A virus RNA synthesis. *Nat Microbiol* **1**, 16029 (2016).
22. Killip, M.J., Fodor, E. & Randall, R.E. Influenza virus activation of the interferon system. *Virus Res* **209**, 11-22 (2015).
23. Te Velthuis, A.J.W. et al. Mini viral RNAs act as innate immune agonists during influenza virus infection. *Nat Microbiol* **3**, 1234-1242 (2018).

## FIGURE LEGENDS

**Fig. 1 Structures of human H3N2 and avian H5N1 FluPol$_A$. a**, Crystal structures of dimers of FluPol$_A$ heterotrimers from human H3N2 (left) and avian H5N1 (right) influenza A viruses. Regions at the dimer interface (shown in close-up in panels **c** and **d**) are boxed. **b**, SEC-SAXS analysis of human H3N2 and avian H5N1 FluPol$_A$ (n=3 independent experiments for H3N2 with similar results and n=1 for H5N1). Smooth lines reflect the relative UV signal of SEC and dotted lines indicate estimated molecular weight for each frame. Note that monomeric FluPol$_A$ heterotrimer has an approximate molecular weight of 255 kDa. **c**, **d,** Interactions between loops 352-356 of the PA C-terminal domains (**c**) and the PA C-terminal

domain and PB2 N1 subdomain (**d**) at the $FluPol_A$ dimer interface. Dashed lines indicate hydrogen bonds.

**Fig. 2 Mutations at the $FluPol_A$ dimer interface inhibit cRNA to vRNA replication. a,** Scheme of transcription and replication by $FluPol_A$ in the context of viral ribonucleoproteins (vRNPs). **b,** vRNP reconstitution assay with the $PA_{352\text{-}356A}$ dimer mutant and complementation with the transcription-deficient $PA_{D108A}$ mutant. Data are mean ± s.e.m., n=3 independent transfections. Two-way ANOVA. $P < 0.05$ is considered significant. mRNA signals for $PA_{352\text{-}356A}$ with and without $PA_{D108A}$ were compared by two-tailed unpaired *t*-test. $P < 0.05$ is considered significant. **c,** Effect of the $PA_{352\text{-}356A}$ mutation on *in vitro* transcription by $FluPol_A$ primed with a capped RNA primer. Data are mean ± s.e.m., n=3 independent reactions. One-way ANOVA. $P<0.05$ is considered significant. **d, e,** Effect of the $PA_{352\text{-}356A}$ mutation on *in vitro* primer-independent replication by $FluPol_A$ on a vRNA (**d**) and cRNA (**e**) template. Data are mean ± s.e.m., n=3 independent reactions. One-way ANOVA. $P < 0.05$ is considered significant. For gel source data, see Supplementary Fig. 2.

**Fig. 3 Structures of H3N2 $FluPol_A$ bound to cRNA promoter. a,** Cryo-EM map of dimer of $FluPol_A$ heterotrimers bound to cRNA promoter. **b,** Cryo-EM map of cRNA-bound $FluPol_A$ heterotrimer in complex with Nb8205. **c,** Close-up view of 3′ cRNA binding site. **d,** Comparison between monomeric (full colour) and dimeric (transparency) $FluPol_A$ polymerase reveals movement of the PB1 thumb/PB2 N1 subdomains (indicated by purple arrows) triggered by $FluPol_A$ dimerisation, resulting in the opening of the 3′ cRNA binding site.

**Fig. 4 Nanobody Nb8205 that binds $FluPol_A$ at the dimer interface inhibits cRNA to vRNA replication and virus growth. a,** Effect of nanobodies on $FluPol_A$ activity in a vRNP reconstitution assay. Data are mean ± s.e.m., n=3 independent transfections. Two-way ANOVA. $P < 0.05$ is considered significant. **b,** Effect of nanobody on *in vitro* transcription by $FluPol_A$ primed with a capped RNA primer. Data are mean ± s.e.m., n=3 independent reactions. One-way ANOVA. $P < 0.05$ is considered significant. **c, d,** Effect of nanobody on *in vitro* primer-independent replication by $FluPol_A$ on a vRNA (**c**) and cRNA (**d**) template. Data are mean ± s.e.m., n=3 independent reactions. One-way ANOVA. $P < 0.05$ is considered significant. **e,** Effect of nanobodies on the growth of influenza A/WSN/33 virus and vRNA levels in infected HEK-293T cells. Data are mean ± s.e.m., n=3 independent

transfections and infections. Two-way ANOVA (Nb8210: $P$ = 0.8126; 0.4390; 0.8496; 0.8489, Nb8205: $P$ = 0.1075; 0.0096; 0.0217; 0.9828, for 16, 24, 32, 48 hours post-infection). $P < 0.05$ is considered significant. For gel source data, see Supplementary Fig. 2. **f,** Model for the role of polymerase dimerisation in influenza virus genome replication.

## METHODS

### Cells

Human embryonic kidney 293T (HEK-293T) and Sf9 insect cells were sourced from the Cell Bank of the Sir William Dunn School of Pathology, University of Oxford. HEK-293T cells were maintained in Dulbecco's Modified Eagle Medium (DMEM) and Sf9 cells were maintained in Sf-900 II serum free medium (Gibco). Cell lines have not been authenticated but tested negative for mycoplasma contamination.

### Protein expression and purification

The three subunits of human influenza A/NT/60/1968 (H3N2) and avian influenza A/duck/Fujian/01/2002 (H5N1) virus polymerases were co-expressed in Sf9 cells from codon-optimized genes (GeneArt) cloned into a single baculovirus using the MultiBac system[24]. Mutagenesis of H3N2 $FluPol_A$ was carried out using the QuickChange Primer Design Program (Agilent). The influenza B/Panama/45/90 polymerase subunits were expressed as for $FluPol_A$, however they were cloned into the biGBac system[25] prior to bacmid generation. Expression and purification of wild-type and mutant $FluPol_A$ and $FluPol_B$ were performed as described[8] with minor modifications. Size exclusion chromatography (SEC) was performed using 25 mM HEPES-NaOH, pH 7.5, 500 mM NaCl, and 5% (v/v) glycerol (Buffer A) on a Superdex 200 Increase 10/300 GL column (GE Healthcare). Pooled fractions from SEC were supplemented with 1 mM TCEP and the final product was concentrated to 3-5 mg $ml^{-1}$ and used for crystallisation or flash-frozen in liquid nitrogen and stored at -80 °C until further use. All purification steps were performed at 4 ˚C.

### Generation, expression and purification of nanobodies

Nanobodies targeting H5N1 $FluPol_A$ were generated following established protocols[26]. Plasmids pMESy4 encoding C-terminal $His_6$-tagged nanobodies were transformed into *E. coli* strain WK6, grown in 2x YT medium containing 0.1% glucose, 2 mM $MgCl_2$ and

100 mg ml$^{-1}$ ampicillin at 37 °C until the $A_{600}$ of the sample reached 0.7, and then induced with 1 mM IPTG and incubated overnight at 28 °C. Cells were collected and the periplasmic fraction was extracted using the modified osmotic shock protocol. The periplasmic extract containing nanobody was incubated with Ni-NTA agarose (Qiagen) for 1 h at room temperature. The beads were washed with 20 volumes of 50 mM $K_2HPO_4$:$NaH_2PO_4$, pH 7.0, 1 M NaCl, followed by 30 volumes of 50 mM $K_2HPO_4$:$NaH_2PO_4$, pH 6.0, 1 M NaCl. Nanobodies were eluted by the addition of 15 volumes of 50 mM Na-acetate, pH 4.6, 1 M NaCl. The eluate was neutralised by the addition of 5 volumes of 1 M Tris-HCl, pH 7.5 and concentrated using an Amicon Ultra centrifugal filter unit (Merck Millipore). Nanobodies were further purified on a Superdex 200 Increase 10/300 gel filtration column (GE Healthcare) in 20 mM Tris-HCl, pH 7.5, 150 mM NaCl. Nanobodies were concentrated to 4 mg ml$^{-1}$, flash-frozen and stored at -20 °C.

**Crystallisation, data collection and structure determination**

Initial hits were found in sitting-drop vapour-diffusion experiments[27] at 20 °C in conditions with 0.8-1.2 M phosphate buffer. After optimisation, H3N2 $FluPol_A$ protein was crystallised in the condition of 0.9-1.2 M $K_2HPO_4$/$NaH_2PO_4$, pH 6.7, and H5N1 $FluPol_A$ in the condition of 1 M $K_2HPO_4$/$NaH_2PO_4$, pH 6.9, 0.07% dichloromethane. Crystals appeared within 1-2 hours and grew to full size after 3-4 days. Crystals were cryo-protected by soaking for 10-30 seconds in 25% (v/v) glycerol or 20% (v/v) ethylene glycol in crystallisation buffer before flash-freezing in liquid nitrogen. H3N2 $FluPol_A$ was co-crystallised with nanobody Nb8205, added to $FluPol_A$ in a 1.5 fold molar excess, using the same conditions as for apo $FluPol_A$. Additional nanobody was added during crystal stabilisation and freezing. Diffraction data were collected at -173 °C on beamlines I03 (wavelength 0.9159 Å) and I24 (wavelength 0.9686 Å) (for H3N2 $FluPol_A$) and I04 (wavelength 0.9795 Å) (for H5N1 $FluPol_A$ and H3N2 $FluPol_A$+Nb8205), at the Diamond Light Source, Didcot, UK. Data were processed using XDS[28] and STARANISO[29], using an anisotropic cut-off and the mean *I/σ(I)* value of 1.20 to determine the diffraction-limit surface. The structure of H5N1 $FluPol_A$ was solved by molecular replacement using Phaser-MR[30] as implemented in PHENIX[31] and a search model of the $FluPol_C$ structure[15] (PDB ID: 5D98) with the PB2 627 domain deleted from the model. Phases of individual 627 domains were obtained by a second round of molecular replacement. After rigid-body refinement, the structure was rebuilt with COOT[32] and refined with PHENIX[31] and autoBUSTER[33] until R-factor values converged. Translation-libration-

screw (TLS) parameters and 4-fold torsion-angle non-crystallographic symmetry (NCS) were also applied in refinement. The structure of H3N2 $FluPol_A$ was solved by molecular replacement using the structure of H5N1 $FluPol_A$ (this study) as the search model and refined in the same way. To determine the structure of human $FluPol_A$ in complex with nanobody Nb8205, chain N of PDB ID: 3SN6[34] was used as a search model for the nanobody. In the final H3N2 $FluPol_A$ model 93.31 % residues are in the most favoured regions of the Ramachandran plot and 0.09 % are in the disallowed regions (90.93 % and 0.08 % for H5N1 $FluPol_A$ model, and 92.65 % and 0 % for H3N2 $FluPol_A$+Nb8205 model, respectively).

**Cryo-EM sample preparation**

Purified dimer fraction of H3N2 $FluPol_A$ was mixed with a 1.2 fold molar excess of 5′ and 3′ cRNA promoters (5′ cRNA: 5′-pAGCAAAAGCAGGCC-3′; 3′ cRNA: 5′-GGCCUUGUUUCUACU-3′) or vRNA promoters (5′ vRNA: 5′-pAGUAGAAACAAGGCC-3′; 3′ vRNA: 5′-GGCCUGCUUUUGCU-3′) and, if stated, a 2.5 fold molar excess of purified nanobody Nb8205 to prepare cRNA-bound $FluPol_A$-nanobody complex. The samples were injected on a Superdex 200 Increase 10/300 GL column (GE Healthcare) running in 25 mM HEPES-NaOH, pH 7.5, 500 mM NaCl. The fractions of interest were concentrated, and protein surface charges were neutralized by adding 0.001% glutaraldehyde for 20 min on ice in order to minimize preferential orientation of particles. After quenching the reaction by adding Tris-HCl, pH 8.0 to a final concentration of 100 mM, the sample was re-injected on a Superdex 200 Increase 10/300 GL column (GE Healthcare) running in 25 mM HEPES-NaOH, pH 7.5, 500 mM NaCl. The fractions of interest were concentrated to 1 mg $ml^{-1}$ and diluted three fold into 25 mM HEPES-NaOH, pH 7.5, 37.5 mM NaSCN, 0.0075% (v/v) Tween 20 prior to grid preparation. A volume of 3.5 µl of cRNA-bound $FluPol_A$ at a concentration of 0.35 mg $ml^{-1}$ was placed on glow discharged carbon-coated (40 nm film) copper C-flat grids (Protochips) with 2 µm holes and 1.0 µm spacing before blotting for 3.5 s and flash-freezing in liquid ethane. Purified dimer fraction of $FluPol_B$ was mixed with a 1.2 fold molar excess of 5′ and 3′ cRNA promoters (5′ cRNA: 5′-pAGCAAAAGCAGGCC-3′; 3′ cRNA: 5′-GGCCUUGUUUCUACU-3′) and the sample was processed as described for $FluPol_A$ and concentrated to 0.35 mg $ml^{-1}$. A volume of 3.5 µl of cRNA-bound $FluPol_B$ was used to prepare grids as described above. All grids were prepared using a Vitrobot mark IV (FEI) at 95-100% humidity.

**Cryo-EM image collection and processing**

Cryo-EM data were collected on a 300 kV Titan Krios microscope (Thermo Fisher Scientific) fitted with a GIF Quantum energy filter (Gatan) at either the Division of Structural Biology (Strubi) or Electron Bio-Imaging Centre (eBIC). For the $FluPol_A$ data sets a Volta Phase Plate (Thermo Fisher Scientific) was used. Micrographs were recorded in counting mode using a K2 Summit (Gatan) direct electron detector (or K3 for the $FluPol_A$-vRNA dataset). For sample-specific data collection parameters, see Extended Data Table 2. Movie data were processed using MotionCor2-1.1.0[35], with a 5 by 5 patch-based alignment, keeping all the frames and dose weighting up to the total exposure. The contrast transfer function and additional phase-shift of full dose non-weighted micrographs was estimated using Gctf-v1.18 or Gctf-v1.06[36] for the $FluPol_B$ dataset. Poor-quality images were discarded after manual inspection. For cRNA-bound dimeric $FluPol_A$, 56,070 particles were manually picked from the dose-weighted micrographs using the RELION 3.0[37] manual picking tool, then extracted in a 250 pixel box and subjected to one round of 2D classification resulting in 16 classes with 43,316 selected particles. 3D classification with alignment into three different classes was performed. Two of the classes containing a total number of 36,913 particles were selected and refined to 4.2 Å with C2 symmetry. Bayesian polishing and per particle CTF refinement were performed in RELION 3.0 improving map resolution up to 4.07 Å. The same particles were also refined without symmetry resulting in a map with a resolution of 4.34 Å. Local resolution estimation and sharpening was performed by the RELION sharpening tool using a -100 $Å^2$ and -80 $Å^2$ B-factor, respectively. For the cRNA-bound $FluPol_A$-Nb8205 complex, a first of set of 406,945 particles has been automatically picked with the template picker implemented in cryoSPARC v2.5[38] using 2D classes from cRNA-bound $FluPol_A$ as a template and then 2D classified. A final set of 34,162 particles containing only the dimeric form of the complex has been exported to RELION 3.0 in a 250 pixel box while the monomeric classes have been used as template for another round of automatic picking. From an initial set of 505,860 particles, 216,066 particles containing only the monomeric form were selected after 2D classification and exported into RELION 3.0 in a 200 pixel box. Both dimer and monomer data sets were refined individually to a resolution at 4.38 Å and 4.1 Å using C1 symmetry, respectively. Bayesian polishing and per particle CTF refinement were performed in RELION 3.0 improving map resolution up to 4.15 Å and 3.79 Å, respectively. For the vRNA-bound $FluPol_A$, a first of set of 2,210,168 particles has been automatically picked with the template picker implemented in cryoSPARC v2.5[38] using 2D classes from cRNA-bound $FluPol_A$ as a template and then 2D classified. A final set of 432,160 particles containing only the monomeric form of the complex has been exported to RELION 3.0 in a

250 pixel box. The data were refined to a resolution at 3.3 Å using C1 symmetry. Bayesian polishing and per particle CTF refinement were performed in RELION 3.0 improving map resolution up to 2.9 Å. A final iteration of 3D classification was performed in RELION 3.0, giving a final map at a resolution of 3.01 Å with a final set of 170,144 particles. For cRNA-bound $FluPol_B$, a first of set of 1,012,085 particles was automatically picked with the template picker implemented in cryoSPARC v2.5[38] using 2D classes of the cRNA-bound $FluPol_A$-Nb8205 complex as a template. After 2D classification, the best views were selected for another round of automatic picking. From an initial set of 324,395 particles, 41,549 particles were selected after 3D classification and exported to RELION 3.0 in a 200 pixel box. The data were refined to a resolution at 4.18 Å using C1 symmetry. The structures were modelled by first fitting an initial model into the locally sharpened map using UCSF Chimera[39]. One cycle of rigid body real space refinement followed by manual adjustment in Coot[40] was performed to correctly position the Cα chain into the density. Finally, cycles of PHENIX[31] real space refinement and manual building in Coot[40] were used to improve model geometry. Map-to-model comparison in PHENIX mtriage validated that no over-fitting was present in the structures. Model geometry was validated for all models using MolProbity[41]. All map and model statistics are detailed in Extended Data Table S2.

**Analytical size-exclusion chromatography (SEC)**

Analytical SEC experiments were performed on a Superdex 200 Increase 10/300 GL column (GE Healthcare) using Buffer A. Wild-type or mutant $FluPol_A$ were loaded via a 100 µl sample loop at a concentration of 10 µM. For investigating the effect of nanobodies, the nanobody was added to $FluPol_A$ in a 1.5 fold molar excess and incubated on ice for one hour before injection.

**Size-exclusion chromatography coupled small-angle X-ray scattering (SEC-SAXS)**

SEC-SAXS experiments were performed on beamline B21 at the Diamond Light Source, Didcot, UK. 45 µl purified $FluPol_A$ at a concentration of 12 µM was injected on a Shodex KW-403 size exclusion column under a flow rate of 0.16 ml $min^{-1}$ at 20˚C in Buffer A. Data were collected using continuous 3 second exposures. The data were buffer-subtracted, scaled, merged, and analysed using the ScÅtter 3.0 software (http://www.bioisis.net/scatter). Molecular weight of each individual frame was estimated from DATASW[42].

**Size-exclusion chromatography coupled multi-angle light scattering (SEC-MALS)**

SEC-MALS experiments were performed on beamline B21 at the Diamond Light Source, Didcot, UK. 45 µl purified $FluPol_A$ at a concentration of 4 µM was injected on a Shodex KW-403 size exclusion column under a flow rate of 0.16 ml $min^{-1}$ at 20˚C in Buffer A in the absence of glycerol. An 18-angle multi-angle light scattering instrument (DAWN HELEOS, WYATT) was used to collect light scattering data and the data were processed with ASTRA (WYATT).

**Plasmids**

Plasmids pcDNA-PB1, pcDNA-PB1a, pcDNA-PB1-FLAG, pcDNA-PB1-TAP (PB1 fused to a C-terminal tandem affinity purification [TAP] tag that consists of a calmodulin binding domain [CBD], a tobacco etch virus [TEV] protease cleavage site, and two copies of protein A), pcDNA-PB2, pcDNA-PB2-TAP, pcDNA-PA, pcDNA-$PA_{D108A}$, pcDNA-NP and pPOLI-NA have been described[12,43-47]. Plasmids pcDNA-$PB2_{71-73A}$, pcDNA-$PA_{351-353A}$, pcDNA-$PA_{356-358A}$, and pcDNA-$PA_{352-356A}$, encoding mutant PB2 and PA polymerase subunits, were generated from pcDNA-PB2 and pcDNA-PA using site-directed PCR mutagenesis. Plasmids pcDNA-Nb8205 and pcDNA-Nb8210, to express nanobodies Nb8205 and Nb8210 in mammalian cells, were generated by PCR amplification using pMESy4 plasmids as templates and cloning into pcDNA3A.

**$FluPol_A$ dimerisation assay**

Dimerisation of $FluPol_A$ in human embryonic kidney 293T (HEK-293T) cells was assessed as described[48]. Protein complexes were analysed by SDS-PAGE and silver staining using SilverXpress (Invitrogen) and bands of PB1-FLAG and PB1-CBD quantitated in ImageJ[49].

**RNP reconstitution assay and primer extension analysis**

Approximately $0.2x10^6$ HEK-293T cells were transfected with 0.2 µg of each pcDNA plasmid encoding PB1, PB2, PA, NP and pPOLI plasmid encoding neuraminidase (NA) vRNA segment, using Lipofectamine 2000 (Invitrogen) according to the manufacturer's instructions. Plasmids encoding mutant proteins or nanobodies were included as indicated. For the complementation assay with a transcription-deficient but replication-competent $PA_{D108A}$ polymerase equal amounts of pcDNA-$PA_{D108A}$ and pcDNA-$PA_{356-358A}$ were co-transfected as described previously[13,48]. Cells were harvested 20 hours post-transfection and total cellular RNA was extracted using TRI reagent (Sigma) according to the manufacturer's instructions. Viral RNA levels were analysed using primer extension as described[50]. Briefly,

RNA was reverse transcribed using $^{32}$P-labelled primers specific to positive and negative sense viral RNAs, with a primer specific to cellular 5S rRNA as a loading control. Transcripts were separated by 6% denaturing PAGE and visualised by phosphorimaging on an FLA-5000 scanner (Fuji). Analysis was carried out using ImageJ[49] and Prism 7 (GraphPad). Viral RNA levels were normalised to the 5S rRNA loading control.

**Virus growth analysis**

Approximately $10^6$ HEK-293T cells were transfected with 5 μg of pcDNA plasmid encoding Nb8205, Nb8210, or an empty pcDNA3 vector using Lipofectamine 2000 (Invitrogen) according to the manufacturer's instructions. 24 hours post-transfection, cells were infected with influenza A/WSN/33 virus at an MOI 0.1. Media was collected 12, 24, 36 and 48 hours post-infection, and virus titres were determined by plaque assay. At each time point, total cellular RNA was also extracted using TRI reagent (Sigma) and vRNA levels were analysed by primer extension[50].

***In vitro* transcription assays**

*In vitro* transcription assays were carried out as described[21]. Briefly, a cap-1 structure was added to a synthetic 11-nucleotide RNA (5′-ppGAAUACUCAAG-3′) (ChemGenes) by mixing 1 μM of RNA with 0.25 μM [α-$^{32}$P]GTP (3000 Ci mmol$^{-1}$; Perkin-Elmer), 0.8 mM S-adenosylmethionine, 0.5 U μl$^{-1}$ vaccinia virus capping enzyme (NEB) and 2.5 U μl$^{-1}$ 2′-O-methyltransferase (NEB) in a 20 μl reaction at 37 °C for 1 hour. The product was isolated by 16% denaturing PAGE, excised, eluted overnight in $dH_2O$, and desalted using NAP-10 columns (GE Healthcare). Transcription reactions were performed using 1,500 c.p.m. capped RNA primer in a 3 μl reaction mixture containing 1mM ATP, 0.5 mM CTP, 0.5 mM UTP, 0.1 μM GTP, 5 mM $MgCl_2$, 1 mM DTT, 2 U μl$^{-1}$ RNasin, 0.5 μM 5′ vRNA promoter, 0.5 μM 3′ vRNA promoter, 70 ng Nb8205 (if indicated) and 100 ng H3N2 $FluPol_A$. Reactions were incubated for 10 min at 30 °C and stopped by the addition of an equal volume of 80% formamide, 1 mM EDTA, and bromophenol blue and xylene cyanol dyes, followed by incubation at 95 °C for 3 min. Products were resolved by 20% denaturing PAGE and visualised by phosphorimaging on an FLA-5000 scanner (Fuji). Analysis was carried out using ImageJ[49] and Prism 7 (GraphPad).

***In vitro* replication assays**

Primer-independent and ApG extension assays were carried out as described[21]. Briefly, 3 µl reaction mixtures containing 1 mM ATP, 0.5 mM CTP, 0.5 mM UTP (if indicated), 0.1 µM GTP, 0.05 µM [α-$^{32}$P]GTP (3000 Ci mmol$^{-1}$; Perkin-Elmer), 0.25 mM ApG (if indicated), 5 mM $MgCl_2$, 1 mM DTT, 2 U µl$^{-1}$ RNasin, 0.5 µM 5′ vRNA or cRNA promoter, 0.5 µM 3′ vRNA or cRNA promoter, 70 ng Nb8205 (if indicated) and 10-100 ng H3N2 $FluPol_A$ were incubated at 37 °C for 4 hours. Where PB1a active site mutant polymerase was added, the concentrations of 5′ and 3′ cRNA promoters were adjusted accordingly to maintain a constant molar ratio of promoter to polymerase. Reactions were stopped by addition of an equal volume of 80% formamide, 1 mM EDTA, and bromophenol blue and xylene cyanol dyes, followed by incubation at 95 °C for 3 min. Products were resolved by 20% denaturing PAGE and visualised by phosphorimaging on an FLA-5000 scanner (Fuji). Analysis was carried out using imageJ[49] and Prism 7 (GraphPad).

**Data availability**

All data are available from the corresponding authors and/or included in the manuscript or Supplementary Information. Atomic coordinates have been deposited in the Protein Data Bank with accession codes 6QNW (H3N2 $FluPol_A$), 6QPF (H5N1 $FluPol_A$) and 6QPG (H3N2 $FluPol_A$+Nb8205). Cryo-EM density maps have been deposited in the Electron Microscopy Data Bank with accession codes EMD-4661 (monomeric H3N2 $FluPol_A$+cRNA+Nb8205), EMD-4663 and 4664 (dimeric H3N2 $FluPol_A$+cRNA), EMD-4666 (dimeric H3N2 $FluPol_A$+cRNA+Nb8205), EMD-4660 (monomeric $FluPol_B$+cRNA), and EMD-4986 (monomeric H3N2 $FluPol_A$+vRNA+capped RNA) with the corresponding atomic coordinates deposited in the Protein Data Bank with accession numbers 6QX3, 6QX8, 6QXE, 6QWL, 6RR7, respectively.


24. Bieniossek, C., Imasaki, T., Takagi, Y. & Berger, I. MultiBac: expanding the research toolbox for multiprotein complexes. *Trends in Biochemical Sciences* **37**, 49-57 (2012).
25. Weissmann, F. et al. biGBac enables rapid gene assembly for the expression of large multisubunit protein complexes. *Proc Natl Acad Sci U S A* **113**, E2564-9 (2016).
26. Pardon, E. et al. A general protocol for the generation of Nanobodies for structural biology. *Nat Protoc* **9**, 674-93 (2014).
27. Walter, T.S. et al. A procedure for setting up high-throughput nanolitre crystallization experiments. Crystallization workflow for initial screening, automated storage, imaging and optimization. *Acta Crystallographica Section D-Biological Crystallography* **61**, 651-657 (2005).
28. Kabsch, W. Xds. *Acta Crystallogr D Biol Crystallogr* **66**, 125-32 (2010).

29. Tickle, I.J. et al. STARANISO (http://staraniso.globalphasing.org/cgi-bin/staraniso.cgi). (Cambridge, United Kingdom: Global Phasing Ltd., 2018).
30. Mccoy, A.J. et al. Phaser crystallographic software. *Journal of Applied Crystallography* **40**, 658-674 (2007).
31. Adams, P.D. et al. PHENIX: a comprehensive Python-based system for macromolecular structure solution. *Acta Crystallographica Section D-Biological Crystallography* **66**, 213-221 (2010).
32. Emsley, P. & Cowtan, K. Coot: model-building tools for molecular graphics. *Acta Crystallographica Section D-Biological Crystallography* **60**, 2126-2132 (2004).
33. Smart, O.S. et al. Exploiting structure similarity in refinement: automated NCS and target-structure restraints in BUSTER. *Acta Crystallogr D Biol Crystallogr* **68**, 368-80 (2012).
34. Rasmussen, S.G. et al. Crystal structure of the beta2 adrenergic receptor-Gs protein complex. *Nature* **477**, 549-55 (2011).
35. Zheng, S.Q. et al. MotionCor2: anisotropic correction of beam-induced motion for improved cryo-electron microscopy. *Nat Methods* **14**, 331-332 (2017).
36. Zhang, K. Gctf: Real-time CTF determination and correction. *J Struct Biol* **193**, 1-12 (2016).
37. Scheres, S.H. RELION: implementation of a Bayesian approach to cryo-EM structure determination. *J Struct Biol* **180**, 519-30 (2012).
38. Punjani, A., Rubinstein, J.L., Fleet, D.J. & Brubaker, M.A. cryoSPARC: algorithms for rapid unsupervised cryo-EM structure determination. *Nat Methods* **14**, 290-296 (2017).
39. Pettersen, E.F. et al. UCSF Chimera--a visualization system for exploratory research and analysis. *J Comput Chem* **25**, 1605-12 (2004).
40. Emsley, P., Lohkamp, B., Scott, W.G. & Cowtan, K. Features and development of Coot. *Acta Crystallogr D Biol Crystallogr* **66**, 486-501 (2010).
41. Davis, I.W. et al. MolProbity: all-atom contacts and structure validation for proteins and nucleic acids. *Nucleic Acids Res* **35**, W375-83 (2007).
42. Shkumatov, A.V. & Strelkov, S.V. DATASW, a tool for HPLC-SAXS data analysis. *Acta Crystallogr D Biol Crystallogr* **71**, 1347-50 (2015).
43. Deng, T., Sharps, J., Fodor, E. & Brownlee, G.G. In vitro assembly of PB2 with a PB1-PA dimer supports a new model of assembly of influenza A virus polymerase subunits into a functional trimeric complex. *J Virol* **79**, 8669-74 (2005).
44. Fodor, E. et al. A single amino acid mutation in the PA subunit of the influenza virus RNA polymerase inhibits endonucleolytic cleavage of capped RNAs. *J Virol* **76**, 8989-9001 (2002).
45. Fodor, E. et al. Rescue of influenza A virus from recombinant DNA. *J Virol* **73**, 9679-82 (1999).
46. Fodor, E. & Smith, M. The PA subunit is required for efficient nuclear accumulation of the PB1 subunit of the influenza A virus RNA polymerase complex. *J Virol* **78**, 9144-53 (2004).
47. Vreede, F.T., Jung, T.E. & Brownlee, G.G. Model suggesting that replication of influenza virus is regulated by stabilization of replicative intermediates. *J Virol* **78**, 9568-72 (2004).
48. Nilsson-Payant, B.E., Sharps, J., Hengrung, N. & Fodor, E. The Surface-Exposed PA(51-72)-Loop of the Influenza A Virus Polymerase Is Required for Viral Genome Replication. *J Virol* **92**(2018).
49. Schneider, C.A., Rasband, W.S. & Eliceiri, K.W. NIH Image to ImageJ: 25 years of image analysis. *Nat Methods* **9**, 671-5 (2012).

50. Robb, N.C., Smith, M., Vreede, F.T. & Fodor, E. NS2/NEP protein regulates transcription and replication of the influenza virus RNA genome. *J Gen Virol* **90**, 1398-407 (2009).
51. Reich, S., Guilligay, D. & Cusack, S. An in vitro fluorescence based study of initiation of RNA synthesis by influenza B polymerase. *Nucleic Acids Res* **45**, 3353-3368 (2017).
52. Bussey, K.A. et al. PA residues in the 2009 H1N1 pandemic influenza virus enhance avian influenza virus polymerase activity in mammalian cells. *J Virol* **85**, 7020-8 (2011).
53. Hu, J. et al. The PA-gene-mediated lethal dissemination and excessive innate immune response contribute to the high virulence of H5N1 avian influenza virus in mice. *J Virol* **87**, 2660-72 (2013).
54. Ilyushina, N.A. et al. Adaptation of pandemic H1N1 influenza viruses in mice. *J Virol* **84**, 8607-16 (2010).
55. Kamiki, H. et al. A PB1-K577E Mutation in H9N2 Influenza Virus Increases Polymerase Activity and Pathogenicity in Mice. *Viruses* **10**(2018).
56. Lee, C.Y. et al. Novel mutations in avian PA in combination with an adaptive mutation in PR8 NP exacerbate the virulence of PR8-derived recombinant influenza A viruses in mice. *Vet Microbiol* **221**, 114-121 (2018).
57. Liedmann, S. et al. New virulence determinants contribute to the enhanced immune response and reduced virulence of an influenza A virus A/PR8/34 variant. *J Infect Dis* **209**, 532-41 (2014).
58. Mehle, A., Dugan, V.G., Taubenberger, J.K. & Doudna, J.A. Reassortment and mutation of the avian influenza virus polymerase PA subunit overcome species barriers. *J Virol* **86**, 1750-7 (2012).
59. Neumann, G., Macken, C.A. & Kawaoka, Y. Identification of amino acid changes that may have been critical for the genesis of A(H7N9) influenza viruses. *J Virol* **88**, 4877-96 (2014).
60. Peng, X. et al. Amino Acid Substitutions HA A150V, PA A343T, and PB2 E627K Increase the Virulence of H5N6 Influenza Virus in Mice. *Front Microbiol* **9**, 453 (2018).
61. Slaine, P.D. et al. Adaptive Mutations in Influenza A/California/07/2009 Enhance Polymerase Activity and Infectious Virion Production. *Viruses* **10**(2018).
62. Wu, R. et al. Multiple amino acid substitutions are involved in the adaptation of H9N2 avian influenza virus to mice. *Vet Microbiol* **138**, 85-91 (2009).
63. Xu, G. et al. Prevailing PA Mutation K356R in Avian Influenza H9N2 Virus Increases Mammalian Replication and Pathogenicity. *J Virol* **90**, 8105-14 (2016).
64. Yamaji, R. et al. Mammalian adaptive mutations of the PA protein of highly pathogenic avian H5N1 influenza virus. *J Virol* **89**, 4117-25 (2015).
65. Zhang, Z. et al. Multiple amino acid substitutions involved in enhanced pathogenicity of LPAI H9N2 in mice. *Infect Genet Evol* **11**, 1790-7 (2011).
66. Zhong, G. et al. Mutations in the PA Protein of Avian H5N1 Influenza Viruses Affect Polymerase Activity and Mouse Virulence. *J Virol* **92**(2018).
67. Tan, Y.Z. et al. Addressing preferred specimen orientation in single-particle cryo-EM through tilting. *Nat Methods* **14**, 793-796 (2017).
68. Naydenova, K. & Russo, C.J. Measuring the effects of particle orientation to improve the efficiency of electron cryomicroscopy. *Nat Commun* **8**, 629 (2017).

## MAIN TEXT STATEMENTS


### Acknowledgements

We thank G.G. Brownlee and F. Vreede for plasmids, I. Berger for the MultiBac system and S. Cusack for sharing and discussing unpublished data on the 3′ promoter binding site. We thank K. Harlos and T. Walter for assistance with crystallisation and K. Dent and D. Clare for cryo-EM assistance. We thank G.G. Brownlee, D. Stuart, and A. te Velthuis, as well as members of the Fodor and Grimes laboratories, for helpful comments and discussions. We thank Instruct-ERIC, part of the European Strategy Forum on Research Infrastructures (ESFRI), Instruct-ULTRA (EU H2020 Grant 731005), and the Research Foundation - Flanders (FWO) for support with nanobody discovery. This work was supported by Medical Research Council (MRC) programme grants MR/K000241/1 and MR/R009945/1 (to E.F.), Wellcome Investigator Award 200835/Z/16/Z (to J.M.G.), MRC Studentships (to A.P.W. and I.S.M.), Wellcome Studentship 092931/Z/10/Z (to N.H.). The authors would like to thank Diamond Light source for beamtime (proposals MX10627, MX14744, and MX19946), and for access and support of the cryo-EM facilities at the UK national Electron Bio-Imaging Centre (eBIC) (proposal EM14856), funded by the Wellcome, MRC and BBSRC. Further EM provision was provided through the OPIC electron microscopy facility which was founded by a Wellcome JIF award (060208/Z/00/Z) and is supported by a Wellcome equipment grant (093305/Z/10/Z). Computation used the Oxford Biomedical Research Computing (BMRC) facility, a joint development between the Wellcome Centre for Human Genetics and the Big Data Institute supported by Health Data Research UK and the NIHR Oxford Biomedical Research Centre. Financial support was provided by a Wellcome Trust Core Award (203141/Z/16/Z). The views expressed are those of the author(s) and not necessarily those of the NHS, the NIHR or the Department of Health. Part of this work was supported by Wellcome administrative support grant 203141/Z/16/Z.


### Author contributions

H.F., A.P.W., L.C., J.R.K., J.M.G. and E.F. conceived and designed the study. H.F., L.C., J.R.K., and N.H. carried out cloning of recombinant baculoviruses and protein purification. H.F. J.R.K. performed crystallisations, data collection and analysis, model building and refinement. L.C. and J.R.K. collected and processed electron microscopy data and built and refined models with assistance from D.K. and I.S.M. A.P.W. performed functional assays and analysed data. J.S. performed dimerisation assays in mammalian cells and E.F. analysed the

data. E.P. and J.S. designed and generated Nb8205 and Nb8210 and N.H. performed nanobody expression and purification. J.M.G and E.F. supervised the structural and functional studies, respectively. H.F., A.P.W., L.C., J.R.K, J.M.G. and E.F. wrote the manuscript, with input from all co-authors.

**Competing interests** The authors declare no competing interests.

**Correspondence and requests for materials** should be addressed to J.M.G. or E.F.

## EXTENDED DATA

**Extended Data Fig. 1 Subunit organisation of $FluPol_A$ heterotrimers. a**, **b,** Views of the structure of human H3N2 (**a**) and avian H5N1 (**b**) $FluPol_A$ heterotrimers, coloured according to subunit. **c–e**, Structures of human H3N2 $FluPol_A$ subunits PA (**c**), PB1 (**d**) and PB2 (**e**), coloured and labelled by domain. **f**, Domain maps of each H3N2 $FluPol_A$ subunit. **g-i**, The 2D Fo − mFc electron density maps of $FluPol_A$ dimer interface as shown in Fig. 1c (**g**, stereo view), and 1d (**h**, stereo view), as well as of the complete $FluPol_A$ dimer (**i**), are shown in gray mesh (contoured at 1.5 σ, all from the H3N2 $FluPol_A$ structure model).

**Extended Data Fig. 2 Effect of mutations at the dimer interface on $FluPol_A$ dimerisation and activity. a,** SEC-MALS analysis of wild type and $PA_{352\text{-}356A}$ mutant H3N2 $FluPol_A$ (n=1 independent experiment). Smooth lines reflect the relative UV signal of SEC and dotted lines indicate estimated molecular weight for each frame. Note that monomeric $FluPol_A$ heterotrimer has an approximate molecular weight of 255 kDa. **b,** Effect of $PA_{352\text{-}356A}$ mutation on $FluPol_A$ dimerisation in HEK-293T cells. Data are mean ± s.e.m., n=3 independent transfections. One-way ANOVA. $P < 0.05$ is considered significant. **c,** Effect of mutations designed to destabilise PB2 and PA loops at the $FluPol_A$ dimer interface on $FluPol_A$ activity in a vRNP reconstitution assay. Data are mean ± s.e.m., n=3 independent transfections. Two-way ANOVA. $P < 0.05$ is considered significant. **d, e,** Effect of $PA_{352\text{-}356A}$ mutation on *in vitro* ApG-primer replication by $FluPol_A$ on a vRNA (**d**) and cRNA (**e**) template. **f,** Effect of an active site polymerase mutant (PB1a) on *in vitro* ApG-primer replication by $FluPol_A$ on a cRNA template. Data are mean ± s.e.m., n=4 independent

reactions. **g,** Omitting UTP from *in vitro* ApG-primer replication by $FluPol_A$ on a cRNA template affects the synthesis of the 15 nucleotide full-length vRNA but not of the 12 nucleotide short vRNA indicating that the 12 nucleotide product is derived from internal initiation by the ApG dinucleotide at positions 4 and 5 of the cRNA template. The position in the template at which UTP is required is indicated in red. Representative data from n=2 independent reactions. For gel source data, see Supplementary Fig. 2.

**Extended Data Fig. 3 Single-particle cryo-EM analysis of human H3N2 $FluPol_A$ bound to cRNA promoter. a,** Representative micrograph of cRNA-bound $FluPol_A$ heterotrimer particles embedded in vitreous ice. **b,** Representative 2D class averages. **c,** FSC curves for 3D reconstruction using gold-standard refinement in RELION, indicating overall map resolution of 4.07 Å and the model-to-map FSC. Curves are shown for phase randomisation, unmasked, masked and phase-randomisation-corrected masked maps. **d,** 3D reconstruction locally filtered and coloured according to RELION local resolution. **e,** Angular distribution of particle projections with the cryo-EM map shown in grey. **f,** Cryo-EM density of the PA loop 352-356 at the dimer interface. **g**, Cryo-EM map of cRNA-bound $FluPol_A$ dimer refined without symmetry imposed (C1), revealing an extra density (green) located next to the 3′ end of the 5′ cRNA close to the template entry channel. **h,** Close-up views highlighting cryo-EM extra density (dark green) with the 3′ vRNA strand from the superimposed $FluPol_B$ structure[51] (PDB: 5MSG, light green) inserting into the polymerase active site. Localisation of the 3′ vRNA shows that bases are positioned in the extra density facing the density corresponding to the 3′ end of the 5′ cRNA, suggesting the presence of a promoter RNA duplex region as observed in vRNA-bound $FluPol_B$[51]. The extra density is consistent with the presence of a 3′ cRNA in one of the heterotrimers of the cRNA-bound $FluPol_A$ dimer, oriented towards the polymerase active site.

**Extended Data Fig. 4 The effect of Nb8205 on $FluPol_A$ dimerisation. a,** SDS-PAGE of purified nanobodies (n=1 independent experiment). **B,** Analytical SEC of $FluPol_A$ in complex with nanobodies (n=4 for Nb8205 and n=2 for Nb8210, with similar results). **c,** Effect of nanobodies on $FluPol_A$ dimerisation in HEK-293T cells. Data are mean ± s.e.m., n=4 independent transfections. One-way ANOVA. $P < 0.05$ is considered significant. For gel source data, see Supplementary Fig. 2. **d,** Crystal structure of H3N2 $FluPol_A$ in complex with Nb8205. **e,** Close-up view of $FluPol_A$-Nb8205 interactions. Residues involved in hydrogen

bonding interactions are labelled and hydrogen bonds are indicated with dashed lines. The complementarity determining regions (CDRs) are coloured individually and labelled.

**Extended Data Fig. 5 Single-particle cryo-EM analysis of monomeric and dimeric cRNA-bound human H3N2 FluPol$_A$ heterotrimer in complex with Nb8205. a,** Representative micrograph of cRNA-bound FluPol$_A$ in complex with Nb8205 embedded in vitreous ice. **b,** Representative 2D class averages. **c,** FSC curves for the 3D reconstruction using gold-standard refinement in RELION, indicating overall map resolution of 3.79 Å and 4.15 Å for the monomeric and dimeric FluPol$_A$ form, respectively, and the model-to-map FSC. Curves are shown for phase randomisation, unmasked, masked and phase-randomisation-corrected masked maps. **d, f,** 3D reconstruction locally filtered and coloured according to RELION local resolution for the dimeric (**d**) and monomeric (**f**) form. **e, g,** Angular distribution of particle projections for the dimeric (**e**) and monomeric (**g**) form with the cryo-EM map shown in grey. **h,** Dimer of FluPol$_A$ heterotrimers bound to cRNA promoter and Nb8205 rigid body fitted into the cryo-EM map of dimeric cRNA-bound FluPol$_A$ heterotrimer in complex with Nb8205. **i,** Cryo-EM map of the dimeric cRNA-bound FluPol$_A$ heterotrimer in complex with Nb8205 revealing an extra density (green) located next to the 3′ end of the 5′ cRNA, as observed for the cRNA-bound FluPol$_A$ dimer (Extended Data Fig. 3g, h).

**Extended Data Fig. 6 Single-particle cryo-EM analysis of cRNA-bound FluPol$_B$. a,** Representative micrograph of cRNA-bound FluPol$_B$ heterotrimer particles embedded in vitreous ice **b,** Representative 2D class averages. **c,** 3D reconstruction locally filtered and coloured according to RELION local resolution. **d,** FSC curves for the 3D reconstruction using gold-standard refinement in RELION, indicating overall map resolution of 4.18 Å and the model-to-map FSC. Curves are shown for the phase randomisation, unmasked, masked, phase-randomisation-corrected masked maps. **e,** Angular distribution of particle projections according to cryoSPARC v2.5 non-uniform refinement. **f,** Cryo-EM map of cRNA-bound FluPol$_B$. **g**, Comparison of the dimerisation interface and the 3′ cRNA binding site in H3N2 FluPol$_A$ (PDB: 6QNW and 6QPG). **h,** 3′ cRNA binding site in FluPol$_A$ and FluPol$_B$ overlaps with the previously identified 3′ vRNA binding site in the La Crosse orthobunyavirus polymerase[19] (PDB: 5AMQ). Sites of 3′ vRNA binding at surface of the polymerase in FluPol$_B$ (PDB: 4WRT) and in the polymerase active site for FluPol$_B$ (PDB: 5MSG) are shown for comparison[6,51]. **i,** Comparison of the structure of dimeric FluPol$_A$ to monomeric

786 $FluPol_B$[51] (PDB: 5MSG) reveals a movement of the priming loop that protrudes from the PB1
787 thumb subdomain into the polymerase active site. Resolved PB1 residues closest to the tip of
788 the priming loop, E638 and M656, move away from the corresponding E637 and M655
789 residues in $FluPol_B$ and the polymerase active site, indicated by the end of the 3′ vRNA, by
790 approximately 7 Å.
791
792 **Extended Data Fig. 7 Single-particle cryo-EM analysis of human H3N2 $FluPol_A$ bound**
793 **to vRNA promoter. a,** Representative micrograph of vRNA-bound $FluPol_A$ heterotrimer
794 particles embedded in vitreous ice. **b,** Representative 2D class averages. **c,** FSC curves for 3D
795 reconstruction using gold-standard refinement in RELION, indicating overall map resolution
796 of 3.01 Å and the model-to-map FSC. Curves are shown for phase randomisation, unmasked,
797 masked and phase-randomisation-corrected masked maps. **d,** 3D reconstruction locally
798 filtered and coloured according to RELION local resolution. **e,** Angular distribution of
799 particle projections with the cryo-EM map shown in grey. **f,** Cryo-EM map of vRNA-bound
800 $FluPol_A$ heterotrimer revealing the presence of a fully resolved priming loop. **g,** Close-up
801 views highlighting the stacking of the 3′ vRNA by the priming loop. **h,** Cartoon illustration of
802 the role of polymerase dimerisation in template realignment during replication initiation on a
803 cRNA template. Base-pairing between the 5′ and 3′ cRNA positions bases 4 and 5 of the 3′
804 cRNA next to the catalytic aspartates (PB1 amino acid residues D445 and D446) in the active
805 site to allow internal replication initiation by the synthesis of a pppApG dinucleotide. The
806 priming loop stacks the cRNA template through PB1 amino acid P651 (left panel). Rotation
807 of the PB1 thumb/PB2-N1 domain triggered by polymerase dimerisation results in a
808 movement of the priming loop and backtracking of the stacked template (arrows).
809 Backtracking is also facilitated by an interaction of PB2 amino acid residue R46 with the 3′
810 cRNA introducing a ‘kink’ in the template. Backtracking positions bases 1 and 2 of the
811 cRNA template opposite the pppApG dinucleotide that remains coordinated by the catalytic
812 aspartates. The resulting replication complex is ready to extend the pppApG dinucleotide by
813 incorporating the next incoming NTP (right panel).
814
815 **Extended Data Fig. 8 Effect of Nb8205 on $FluPol_A$ activity and mapping of host**
816 **adaptive mutations at the $FluPol_A$ dimer interface. a, b,** Effect of Nb8205 on *in vitro*
817 ApG-primer replication by $FluPol_A$ on a vRNA (**a**) and cRNA (**b**) template. Data are mean ±
818 s.e.m., n=3 independent reactions. **c,** Omitting UTP from *in vitro* ApG-primer replication by

819 $FluPol_A$ on a cRNA template affects the synthesis of the 15 nucleotide full-length vRNA but
820 not of the 12 nucleotide short vRNA. The position in the template at which UTP is required is
821 indicated in red. Representative data from n=2 independent reactions. For gel source data, see
822 Supplementary Fig. 2. **d,** Crystal structure of H3N2 $FluPol_A$ with amino acid residues
823 implicated in avian to mammalian host adaptation of influenza A viruses indicated[52-66].
824
825 **Extended Table 1. Crystallographic data collection and refinement statistics**
826 *Values in parentheses are for highest-resolution shell.
827 Number of crystals used for each dataset: 4 (6QNW), 1 (6QPF), and 2 (6QPG).
828
829 **Extended Table 2. Cryo-EM data collection, refinement and validation statistics**
830 *Sphericity score calculated from 3D FSC curves[67].
831 **Efficiency score calculated from cryoEF[68].

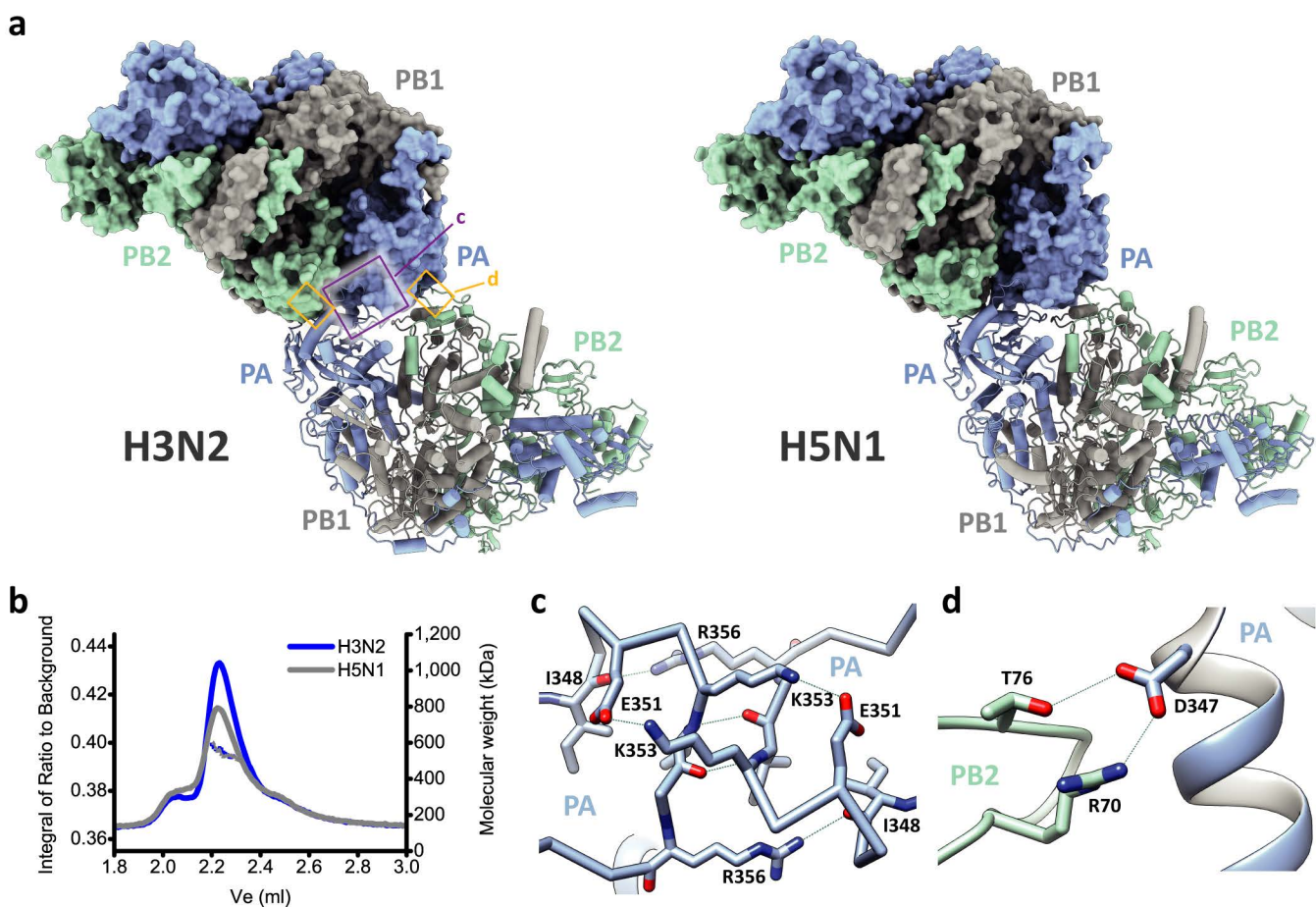
a
PB1
PB2
PA
c
d
PB2
PA
PB1
H3N2
PB1
PB2
PA
PB2
PA
H5N1
PB1
b
Integral of Ratio to Background
0.44
0.42
0.40
0.38
0.36
H3N2
H5N1
1,200
1,000
800
600
400
200
0
Molecular weight (kDa)
1.8
2.0
2.2
2.4
2.6
2.8
3.0
Ve (ml)
c
R356
PA
I348
E351
K353
E351
K353
PA
I348
R356
d
PA
T76
D347
PB2
R70

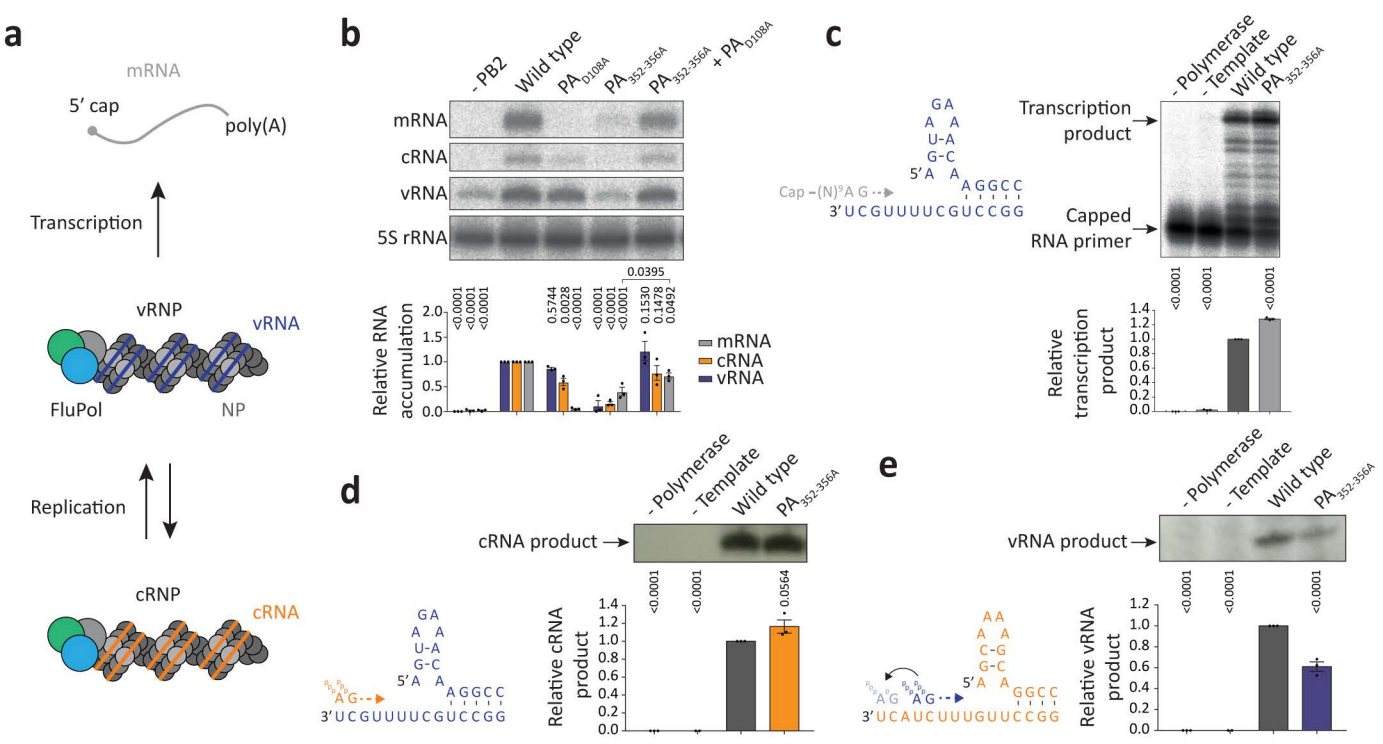
a
mRNA
5′ cap
poly(A)
Transcription
vRNP
vRNA
FluPol
NP
Replication
cRNP
cRNA
b
- PB2
Wild type
PA D108A
PA 352-356A
PA 352-356A
+ PA D108A
mRNA
cRNA
vRNA
5S rRNA
Relative RNA accumulation
<0.0001
<0.0001
<0.0001
0.5744
0.0028
<0.0001
<0.0001
<0.0001
<0.0001
0.0395
0.1530
0.1778
0.0492
mRNA
cRNA
vRNA
c
- Polymerase
- Template
Wild type
PA 352-356A
Transcription product
Capped RNA primer
Cap –(N)9A G
3′UCGUUUUCGUCCGG
Relative transcription product
<0.0001
<0.0001
<0.0001
d
- Polymerase
- Template
Wild type
PA 352-356A
cRNA product
Relative cRNA product
<0.0001
<0.0001
0.0564
3′UCGUUUUCGUCCGG
e
- Polymerase
- Template
Wild type
PA 352-356A
vRNA product
Relative vRNA product
<0.0001
<0.0001
<0.0001
3′UCAUCUUUGUUCCGG

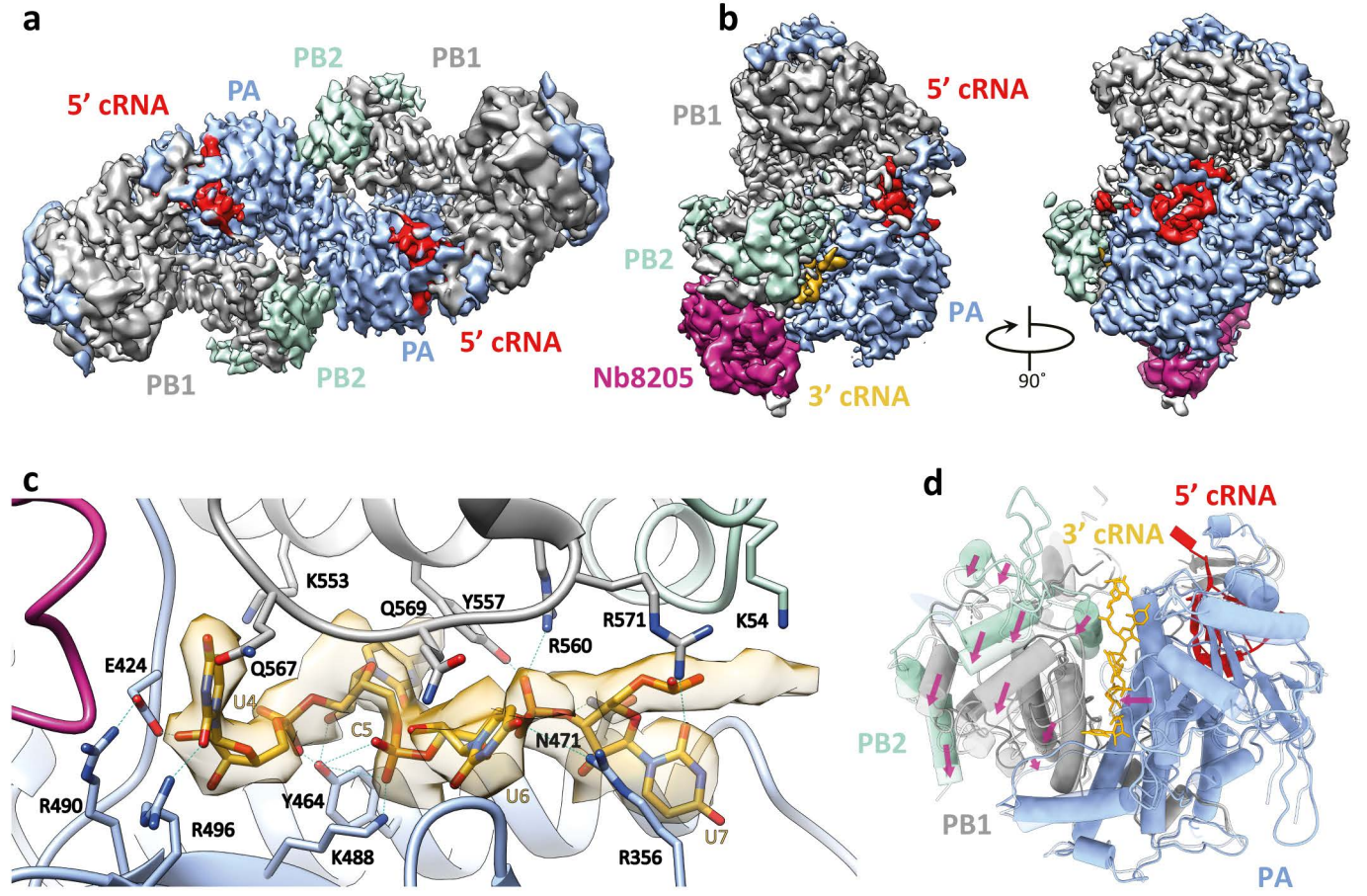
a
PB2
PB1
5′ cRNA
PA
PA
5′ cRNA
PB1
PB2
b
PB1
5′ cRNA
PB2
PA
Nb8205
3′ cRNA
90°
c
K553
Q569
Y557
R571
K54
R560
E424
Q567
U4
C5
N471
R490
Y464
U6
R496
K488
U7
R356
d
5′ cRNA
3′ cRNA
PB2
PB1
PA

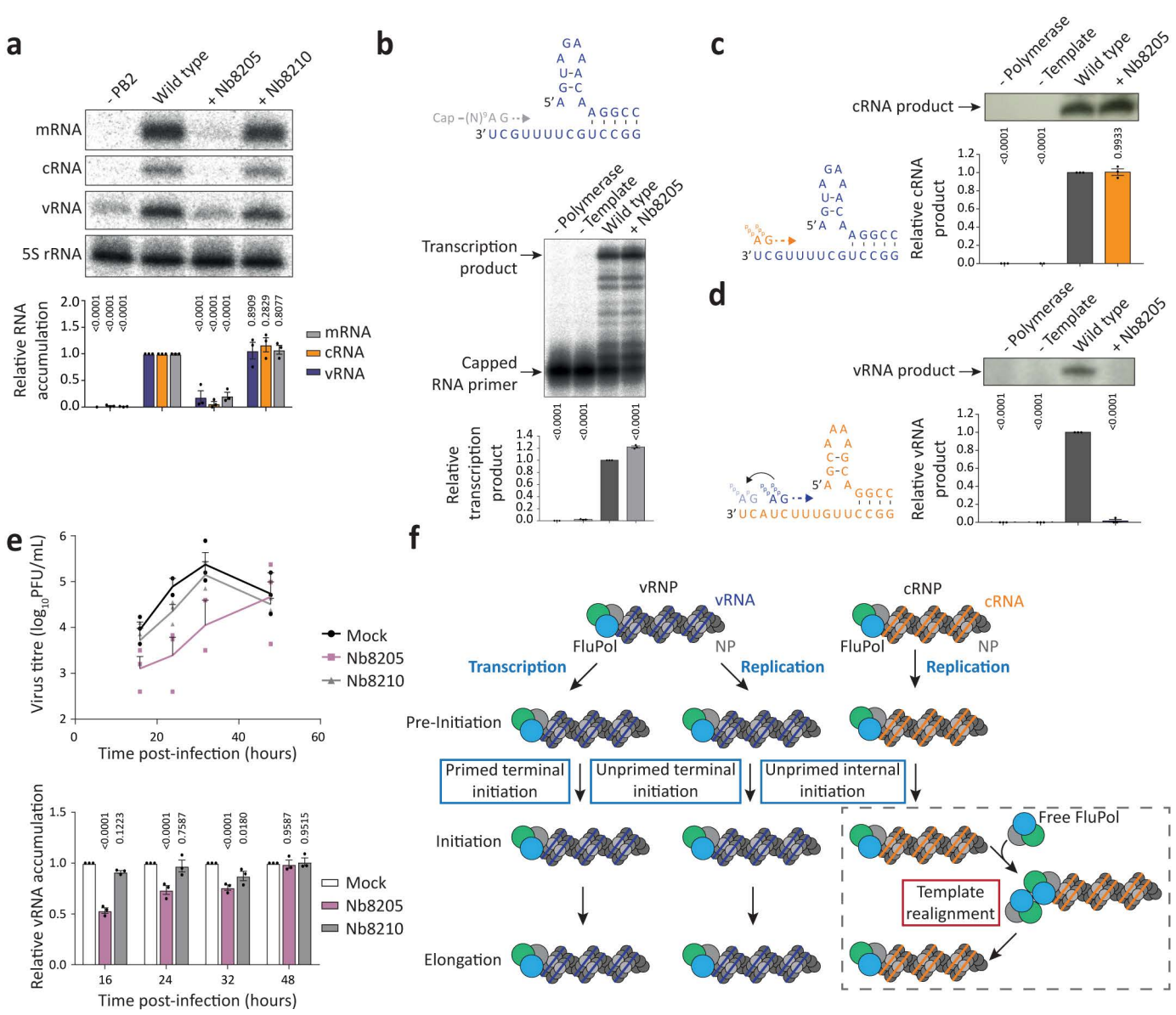
a
- PB2
Wild type
+ Nb8205
+ Nb8210
mRNA
cRNA
vRNA
5S rRNA
Relative RNA accumulation
mRNA
cRNA
vRNA
b
Cap –(N)9A G
3′UCGUUUUCGUCCGG
- Polymerase
- Template
Wild type
+ Nb8205
Transcription product
Capped RNA primer
Relative transcription product
c
- Polymerase
- Template
Wild type
+ Nb8205
cRNA product
Relative cRNA product
d
- Polymerase
- Template
Wild type
+ Nb8205
vRNA product
Relative vRNA product
3′UCAUCUUUGUUCCGG
e
Virus titre (log10 PFU/mL)
Time post-infection (hours)
Mock
Nb8205
Nb8210
Relative vRNA accumulation
Time post-infection (hours)
f
vRNP
vRNA
cRNP
cRNA
FluPol
NP
Transcription
Replication
Pre-Initiation
Primed terminal initiation
Unprimed terminal initiation
Unprimed internal initiation
Initiation
Elongation
Free FluPol
Template realignment

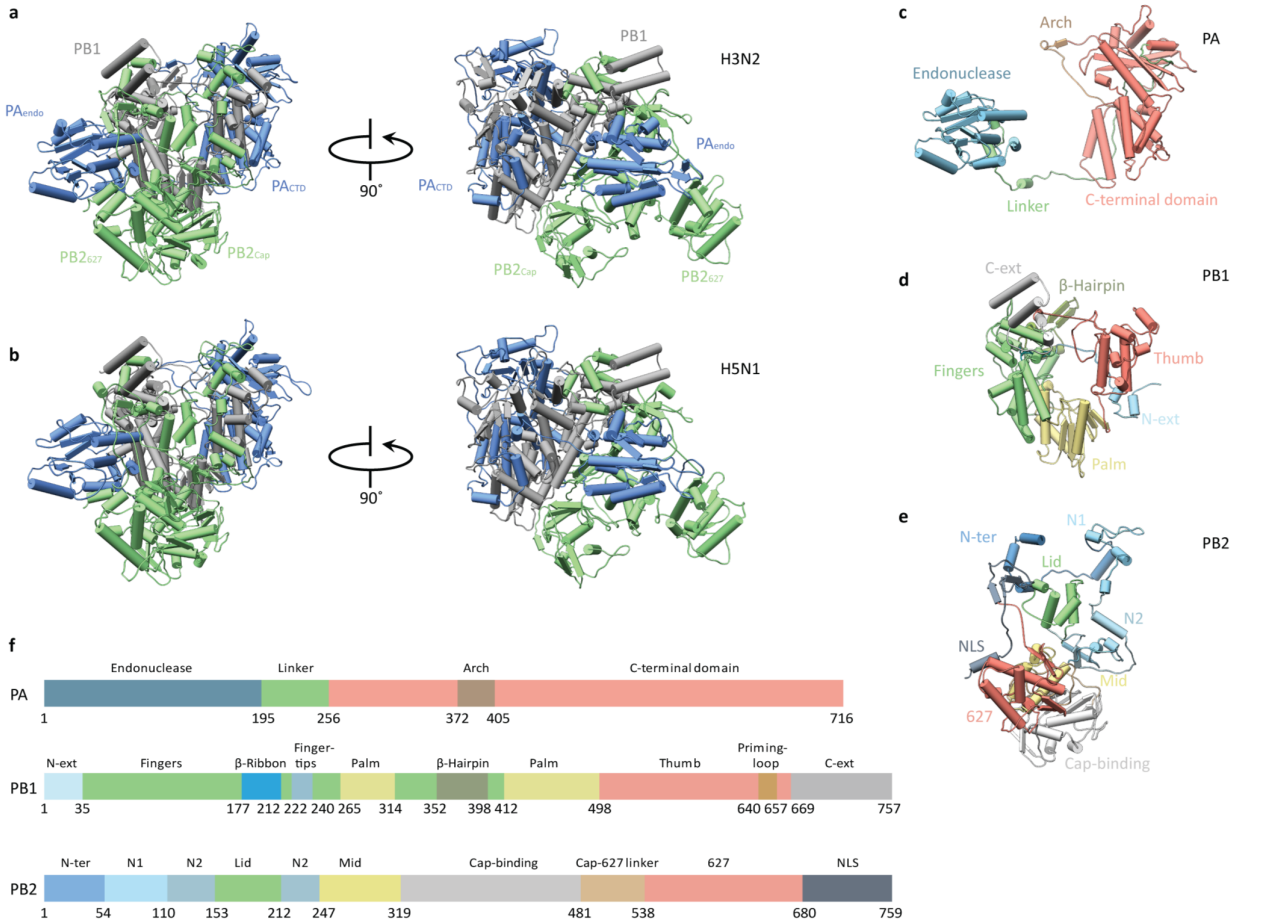
a
PB1
PAendo
PACTD
PB2627
PB2Cap
90˚
H3N2
b
H5N1
c
Arch
PA
Endonuclease
Linker
C-terminal domain
d
PB1
C-ext
β-Hairpin
Fingers
Thumb
N-ext
Palm
e
PB2
N1
N-ter
Lid
N2
NLS
Mid
627
Cap-binding
f
PA
Endonuclease
Linker
Arch
C-terminal domain
1 195 256 372 405 716
PB1
N-ext
Fingers
β-Ribbon
Finger-tips
Palm
β-Hairpin
Palm
Thumb
Priming-loop
C-ext
1 35 177 212 222 240 265 314 352 398 412 498 640 657 669 757
PB2
N-ter
N1
N2
Lid
N2
Mid
Cap-binding
Cap-627 linker
627
NLS
1 54 110 153 212 247 319 481 538 680 759
g
E351
K353
R356
I348
h
T76
R70
D347
i

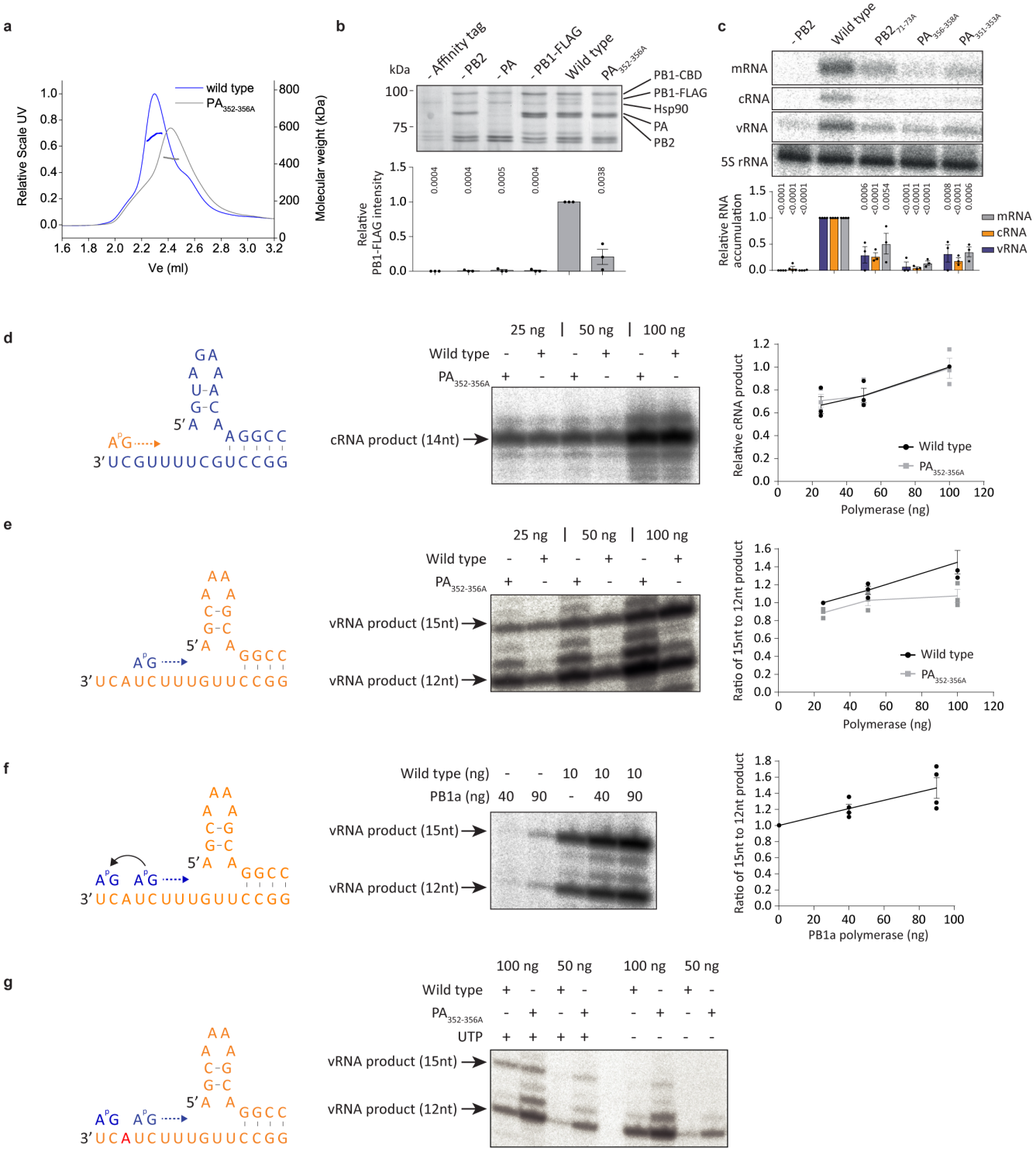
a
wild type
PA352-356A
Relative Scale UV
Molecular weight (kDa)
Ve (ml)
b
kDa
- Affinity tag
- PB2
- PA
- PB1-FLAG
Wild type
PA352-356A
PB1-CBD
PB1-FLAG
Hsp90
PA
PB2
Relative PB1-FLAG intensity
c
- PB2
Wild type
PB2 1-73A
PA 356-358A
PA 351-353A
mRNA
cRNA
vRNA
5S rRNA
Relative RNA accumulation
d
25 ng | 50 ng | 100 ng
Wild type
PA352-356A
cRNA product (14nt)
Relative cRNA product
Polymerase (ng)
e
vRNA product (15nt)
vRNA product (12nt)
Ratio of 15nt to 12nt product
f
Wild type (ng)
PB1a (ng)
PB1a polymerase (ng)
g
100 ng | 50 ng | 100 ng | 50 ng
UTP

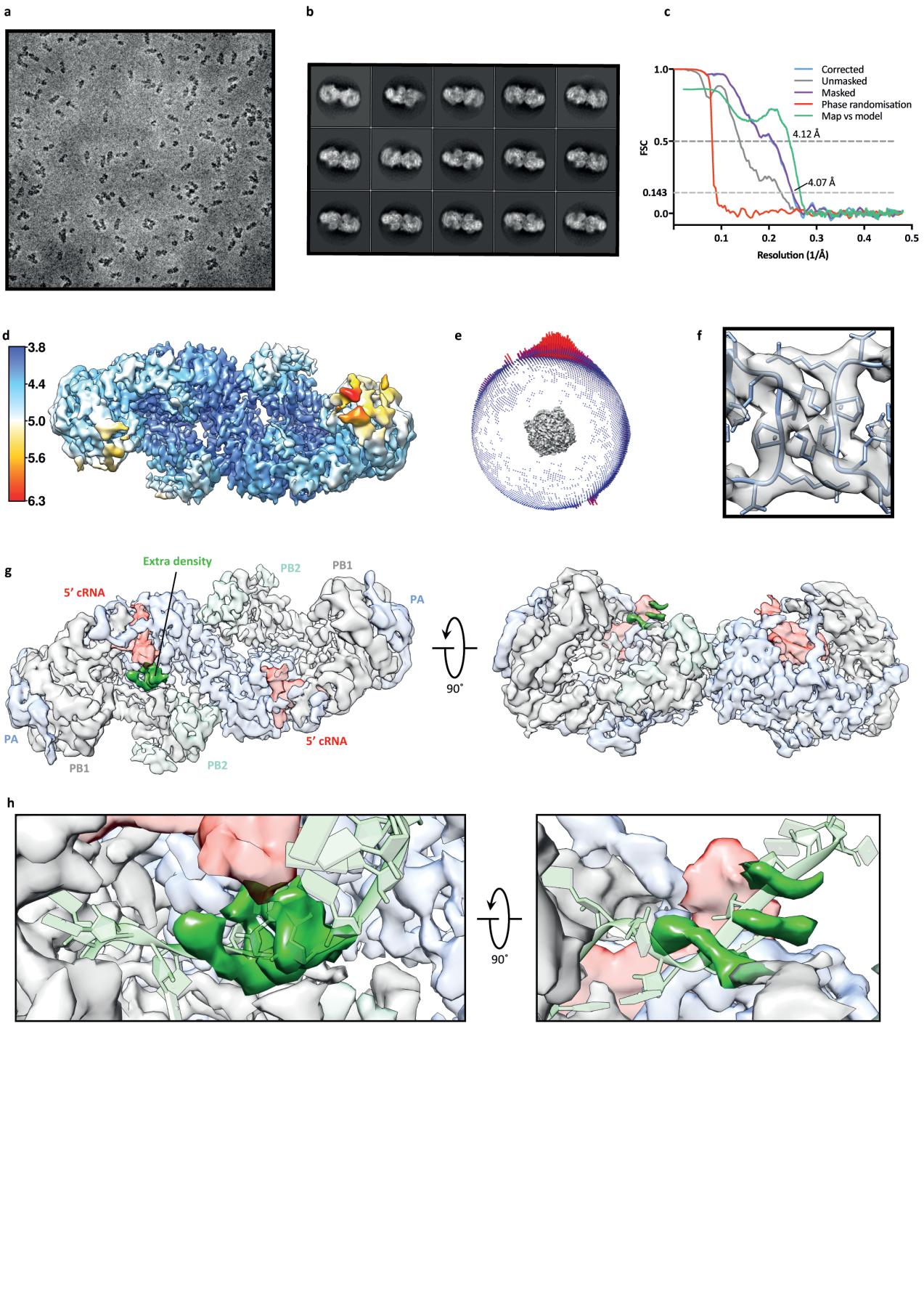
a
b
c
Corrected
Unmasked
Masked
Phase randomisation
Map vs model
4.12 Å
4.07 Å
FSC
1.0
0.5
0.143
0.0
0.1
0.2
0.3
0.4
0.5
Resolution (1/Å)
d
3.8
4.4
5.0
5.6
6.3
e
f
g
Extra density
PB2
PB1
PA
5' cRNA
PA
PB1
PB2
5' cRNA
90˚
h
90˚

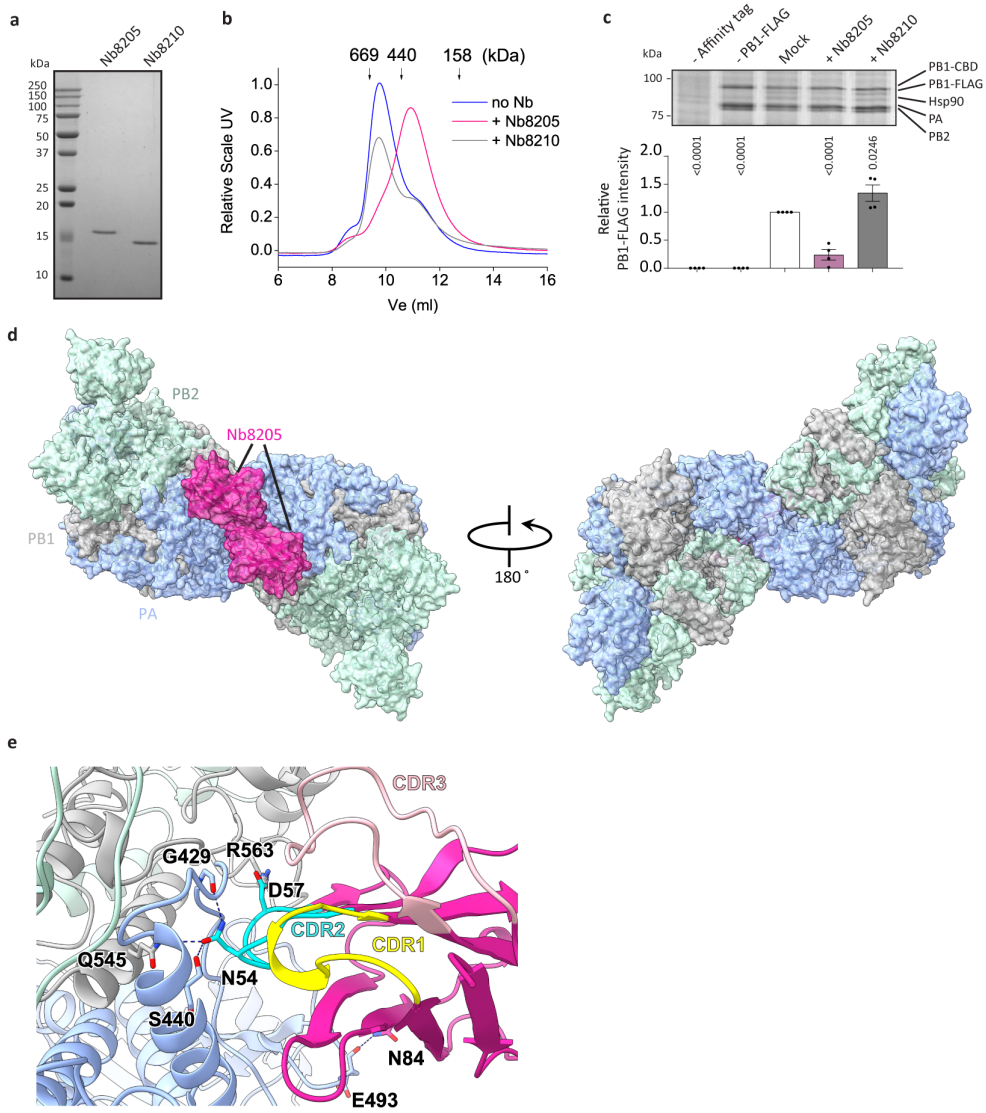
a
kDa
Nb8205
Nb8210
250
150
100
75
50
37
25
20
15
10
b
669 440 158 (kDa)
Relative Scale UV
no Nb
+ Nb8205
+ Nb8210
Ve (ml)
c
kDa
- Affinity tag
- PB1-FLAG
Mock
+ Nb8205
+ Nb8210
PB1-CBD
PB1-FLAG
Hsp90
PA
PB2
Relative PB1-FLAG intensity
<0.0001
<0.0001
<0.0001
0.0246
d
PB2
Nb8205
PB1
PA
180˚
e
CDR3
G429
R563
D57
CDR2
CDR1
Q545
N54
S440
N84
E493

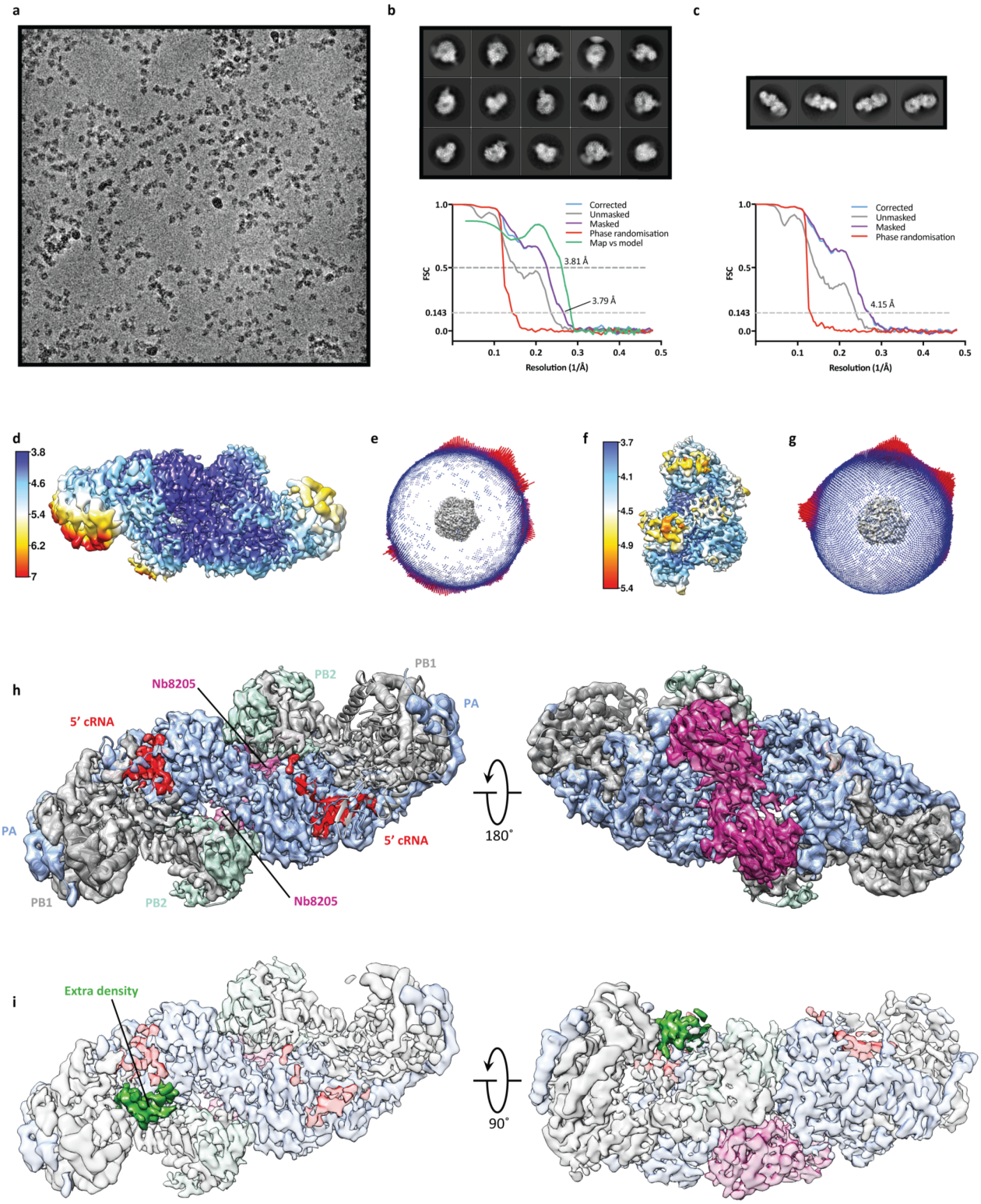
a
b
c
Corrected
Unmasked
Masked
Phase randomisation
Map vs model
3.81 Å
3.79 Å
4.15 Å
FSC
Resolution (1/Å)
d
e
f
g
h
Nb8205
PB2
PB1
PA
5′ cRNA
180˚
i
Extra density
90˚

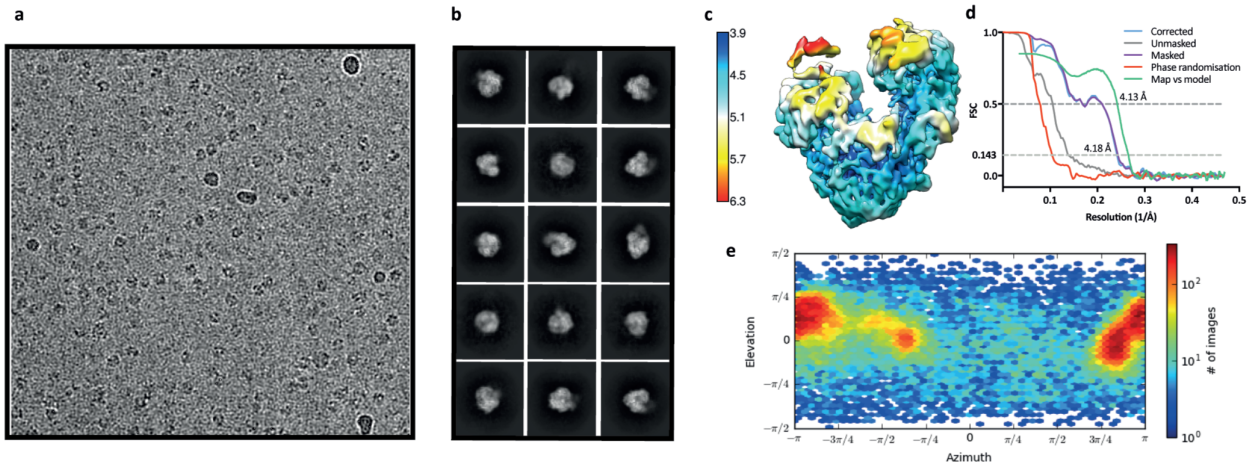
a
b
c
3.9
4.5
5.1
5.7
6.3
d
Corrected
Unmasked
Masked
Phase randomisation
Map vs model
FSC
1.0
0.5
0.143
0.0
4.13 Å
4.18 Å
0.1
0.2
0.3
0.4
0.5
Resolution (1/Å)
e
Elevation
Azimuth
# of images
$10^2$
$10^1$
$10^0$
$\pi/2$
$\pi/4$
0
$-\pi/4$
$-\pi/2$
$-\pi$
$-3\pi/4$
$-\pi/2$
$-\pi/4$
0
$\pi/4$
$\pi/2$
$3\pi/4$
$\pi$

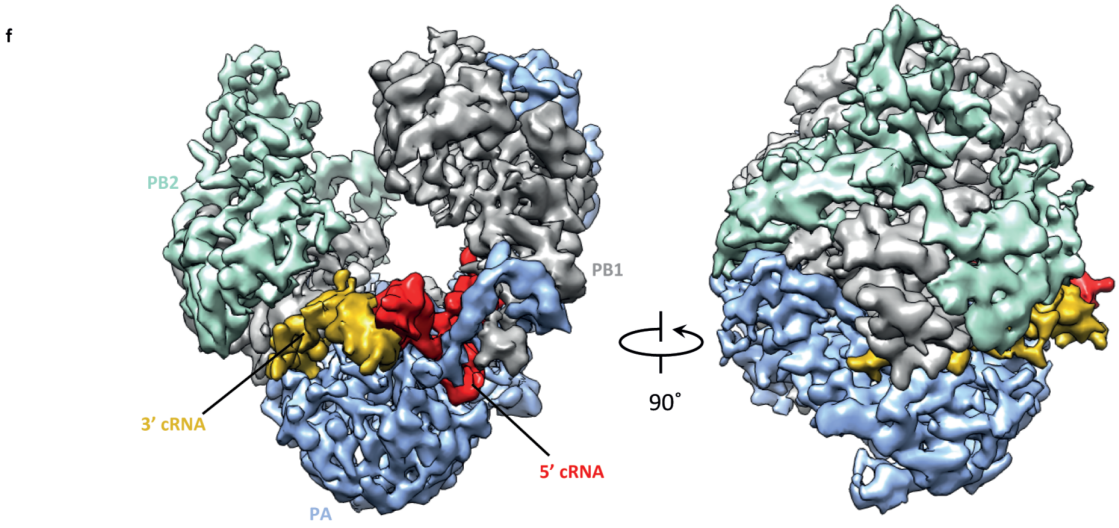
f
PB2
PB1
3′ cRNA
5′ cRNA
PA
90°

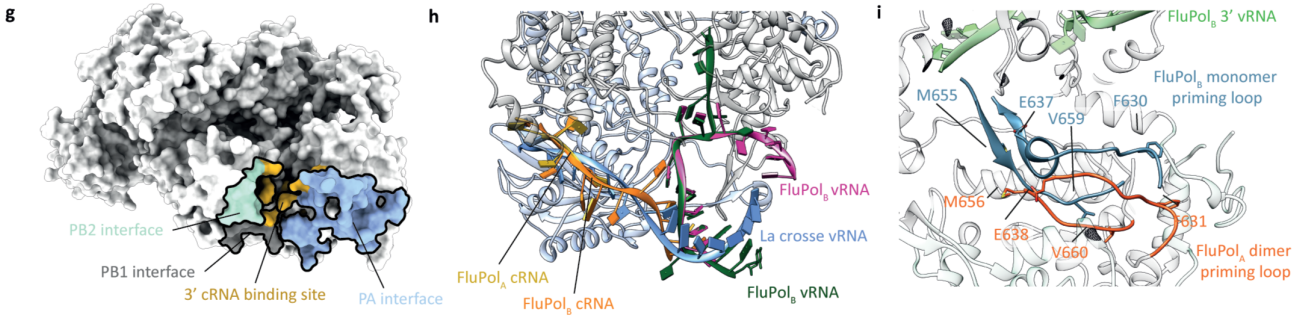
g
PB2 interface
PB1 interface
3′ cRNA binding site
PA interface
h
FluPol$_A$ cRNA
FluPol$_B$ cRNA
FluPol$_B$ vRNA
La crosse vRNA
FluPol$_B$ vRNA
i
FluPol$_B$ 3′ vRNA
FluPol$_B$ monomer priming loop
M655
E637
V659
F630
M656
E638
V660
F631
FluPol$_A$ dimer priming loop

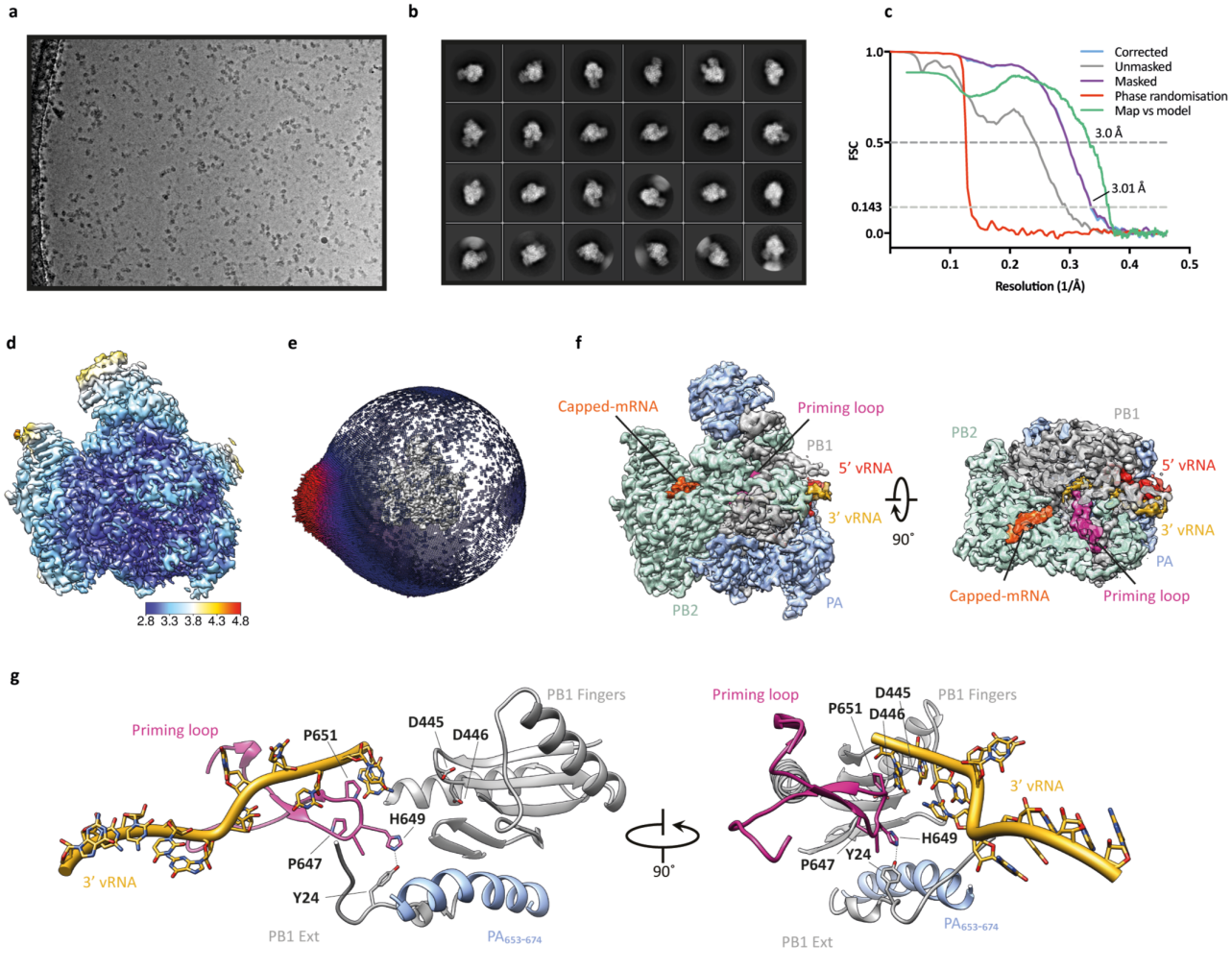
a
b
c
Corrected
Unmasked
Masked
Phase randomisation
Map vs model
3.0 Å
3.01 Å
FSC
1.0
0.5
0.143
0.0
0.1
0.2
0.3
0.4
0.5
Resolution (1/Å)
d
2.8 3.3 3.8 4.3 4.8
e
f
Capped-mRNA
Priming loop
PB1
5′ vRNA
3′ vRNA
90˚
PB2
PA
PB1
PB2
5′ vRNA
3′ vRNA
PA
Capped-mRNA
Priming loop
g
Priming loop
P651
D445
D446
PB1 Fingers
H649
P647
Y24
3′ vRNA
PB1 Ext
PA653-674
90˚
Priming loop
D445
P651
D446
PB1 Fingers
3′ vRNA
H649
P647
Y24
PA653-674
PB1 Ext
h
Priming loop
D445
P651
D446
pppApG
PB1 thumb
R46
PB2 N1
Catalytic site
5′ cRNA
3′ cRNA
PA C-terminus
Priming loop
D445
P651
D446
pppApG
PB1 thumb
R46
PB2 N1
Catalytic site
5′ cRNA
3′ cRNA
PA C-terminus

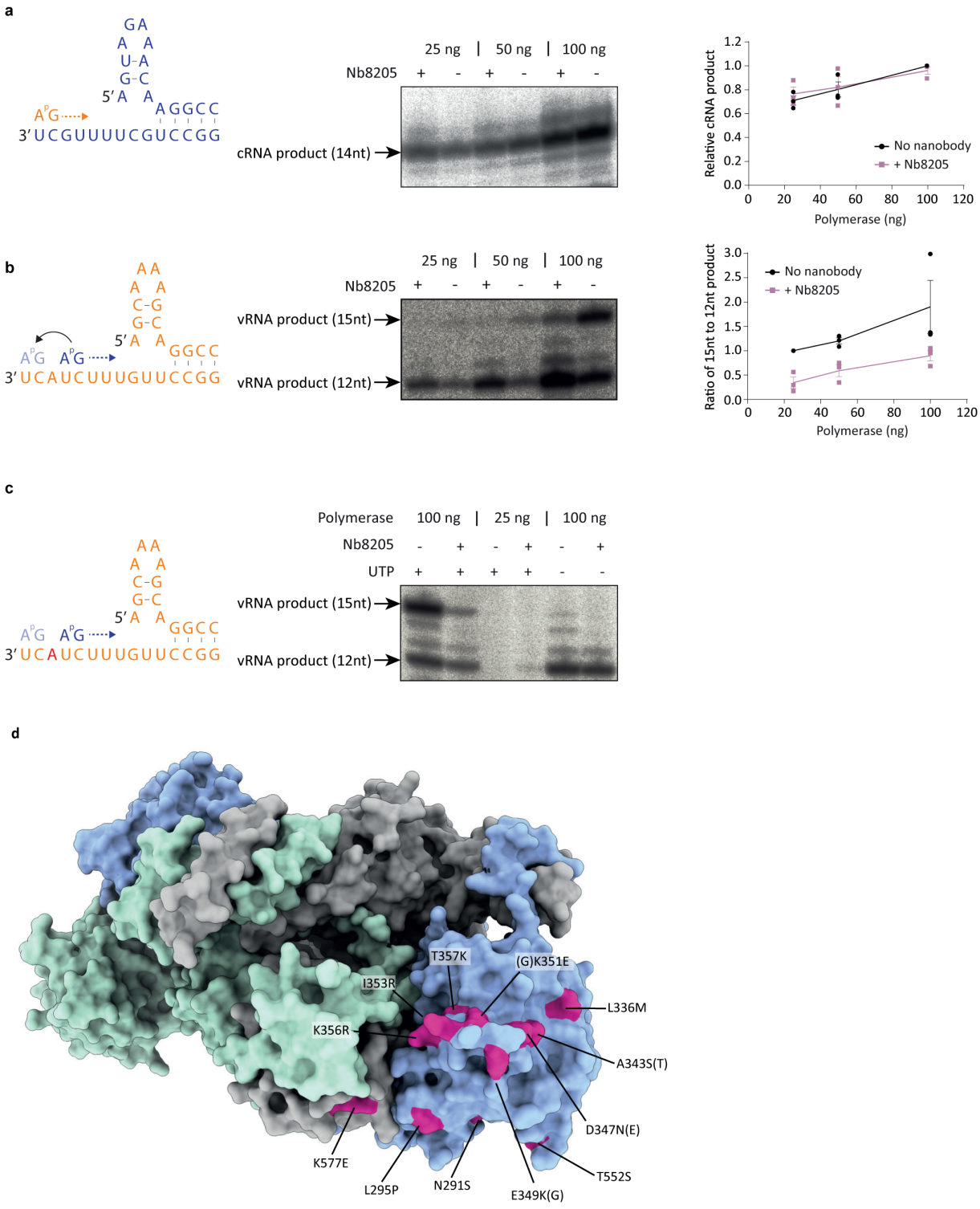
a
25 ng | 50 ng | 100 ng
Nb8205 + - + - + -
cRNA product (14nt)
Relative cRNA product
No nanobody
+ Nb8205
Polymerase (ng)
b
25 ng | 50 ng | 100 ng
Nb8205 + - + - + -
vRNA product (15nt)
vRNA product (12nt)
Ratio of 15nt to 12nt product
No nanobody
+ Nb8205
Polymerase (ng)
c
Polymerase 100 ng | 25 ng | 100 ng
Nb8205 - + - + - +
UTP + + + + - -
vRNA product (15nt)
vRNA product (12nt)
d
T357K
(G)K351E
I353R
L336M
K356R
A343S(T)
D347N(E)
K577E
L295P
N291S
E349K(G)
T552S

| | **H3N2 FluPol$_A$**<br>PDB: 6QNW | **H5N1 FluPol$_A$**<br>PDB: 6QPF | **H3N2 FluPol$_A$-Nb8205**<br>PDB: 6QPG |
|---|---|---|---|
| **Data collection** | | | |
| Space group | C2 | C2 | C2 |
| Cell dimensions | | | |
| *a*, *b*, *c* (Å) | 336.5, 191.9, 235.7 | 337.1, 192.9, 235.7 | 335.2, 192.9, 235.1 |
| α, β, γ (°) | 90.0, 91.5, 90.0 | 90.0, 91.5, 90.0 | 90.0, 91.8, 90.0 |
| Resolution* (Å) | 235.6-3.3 (3.92-3.32) | 235.6-3.6 (4.27-3.63) | 235.0-3.3 (3.87-3.34) |
| $R_{merge}$* (ellipsoidal) | 0.46 (2.24) | 0.18 (0.61) | 0.34 (1.24) |
| $I / \sigma I$* | 4.8 (2.0) | 2.9 (1.6) | 4.8 (1.8) |
| Completeness* (%, ellipsoidal) | 95.3 (80.7) | 92.7 (72.4) | 91.9 (74.5) |
| Redundancy* | 14.4 (13.7) | 3.4 (3.4) | 7.0 (6.9) |
| | | | |
| **Refinement** | | | |
| Resolution (Å) | 135.34-3.32 | 235.61-3.63 | 234.98-3.34 |
| No. reflections | 123,065 | 81,274 | 89,539 |
| $R_{work}$ / $R_{free}$ (%) | 23.5/27.9 | 27.7/32.3 | 25.6/30.1 |
| No. atoms | | | |
| Protein | 67,232 | 67,760 | 70,549 |
| Ligand/ion | 0 | 0 | 0 |
| Water | 0 | 0 | 0 |
| *B*-factors (Å$^2$) | | | |
| Protein | 117.0 | 101.0 | 78.0 |
| Ligand/ion | - | - | - |
| Water | - | - | - |
| R.m.s. deviations | | | |
| Bond lengths (Å) | 0.002 | 0.003 | 0.002 |
| Bond angles (°) | 0.62 | 0.71 | 0.62 |

| | **FluPol$_A$-cRNA** | | **FluPol$_A$-cRNA-Nb8205** | | **FluPol$_B$-cRNA** | **FluPol$_A$-vRNA** |
|---|---|---|---|---|---|---|
| | Dimer | | Monomer | Dimer | Monomer | Monomer |
| | EMD-4664 | EMD-4663<br>PDB 6QX8 | EMD-4661<br>PDB 6QX3 | EMD-4666<br>PDB 6QXE | EMD-4660<br>PDB 6QWL | EMD-4986<br>PDB 6RR7 |
| **Data collection and processing** | | | | | | |
| Magnification | 130,000 | | 130,000 | | 130,000 | 130,000 |
| Voltage (kV) | 300 | | 300 | | 300 | 300 |
| Electron exposure (e–/Å$^2$) | 32.92 | | 30.00 | | 31.10 | 36.60 |
| Defocus range (μm) | -0.5 to -0.7 | | -0.5 to -0.7 | | -1.3 to -2.5 | -0.5 |
| Pixel size (Å) | 1.043 | | 1.080 | | 1.080 | 1.085 |
| Symmetry imposed | C1 | C2 | C1 | C1 | C1 | C1 |
| Initial particle images (no.) | 56,070 | | 505,860 | 406,945 | 1,012,085 | 2,210,168 |
| Final particle images (no.) | 36,913 | | 52,932 | 27,861 | 41,549 | 170,144 |
| Map resolution (Å)<br>(FSC threshold 0.143) | 4.34 | 4.07 | 3.79 | 4.15 | 4.18 | 3.01 |
| Map resolution range (Å) | 3.97-7.82 | 3.84-6.35 | 3.70-5.41 | 3.85-7.43 | 3.90-6.30 | 2.82-5.03 |
| 3DFSC spherity* | 0.758 | 0.787 | 0.851 | 0.772 | 0.781 | 0.909 |
| CryoEF score** | 0.41 | 0.53 | 0.72 | 0.50 | 0.68 | 0.50 |
| | | | | | | |
| **Refinement** | | | | | | |
| Initial model used (PDB code) | - | 6QNW | 6QPG | 6QX8/6QPG | 5EPI | 6QNW |
| Model resolution (Å)<br>(FSC threshold 0.143) | 4.34 | 4.07 | 3.79 | 4.15 | 4.18 | 3.01 |
| Model resolution range (Å) | 3.97-7.82 | 3.84-6.35 | 3.70-5.41 | 3.85-7.43 | 3.90-6.30 | 2.82-5.03 |
| Map sharpening *B* factor (Å$^2$) | -80 | -100 | -110 | -95 | -57 | -65 |
| Model composition | | | | | | |
| Non-hydrogen atoms | - | 38,596 | 21,589 | - | 10,409 | 36,306 |
| Protein residues | - | 2,384 | 1,337 | - | 1,244 | 2,228 |
| Nucleotide (RNA) | - | 24 | 14 | - | 26 | 30 |
| *B* factors (Å$^2$) | | | | | | |
| Protein | - | 68.60 | 71.24 | - | 151.24 | 22.39 |
| Nucleotide (RNA) | - | 64.94 | 86.46 | - | 207.12 | 24.68 |
| R.m.s. deviations | | | | | | |
| Bond lengths (Å) | - | 0.007 | 0.004 | - | 0.008 | 0.007 |
| Bond angles (°) | - | 1.158 | 0.750 | - | 1.006 | 0.820 |
| Validation | | | | | | |
| MolProbity score | - | 1.85 | 1.66 | - | 2.10 | 1.31 |
| Clashscore | - | 6.48 | 3.24 | - | 10.07 | 1.90 |
| Poor rotamers (%) | - | 0.14 | 0 | - | 0.93 | 0 |
| Ramachandran plot | | | | | | |
| Favored (%) | - | 91.86 | 90.34 | - | 89.07 | 94.88 |
| Allowed (%) | - | 7.97 | 9.66 | - | 10.85 | 5.12 |
| Disallowed (%) | - | 0.17 | 0 | - | 0.08 | 0 |